International Journal of Coal Geology 296 (2024) 104658

Contents lists available at ScienceDirect

International Journal of Coal Geology

journal homepage: www.elsevier.com/locate/coal

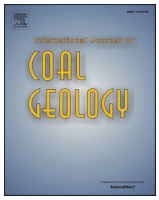

Organic petrology and geochemistry of the late Neogene Shizigou Formation in the Qaidam Basin, China: Characteristics of a prospective microbial gas source rock

Jinqi Qiao [a,b], Qingyong Luo [a,b,*], Shouxin Guo [a,b], Xianglu Tang [a,c], Ludmila Kopaevich [d], Ralf Littke [e]

[a] Key Laboratory of Shale Gas Exploration, Ministry of Natural Resources, China University of Petroleum, Beijing 102249, China
[b] Basin and Reservoir Research Center, China University of Petroleum, Beijing 102249, China
[c] Unconventional Natural Gas Research Institute, China University of Petroleum, Beijing 102249, China
[d] Lomonosov Moscow State University, GSP-1, Leninskie Gory, Moscow 119991, Russia
[e] Energy and Mineral Resources Group (EMR), Institute of Organic Biogeochemistry in Geosystems, RWTH Aachen University, Lochnerstr. 4-20, 52056 Aachen, Germany

ARTICLE INFO

Keywords:
Upper Neogene
Organic petrology
Molecular characteristics
Microbial gas source rocks
Yiliping Depression
Qaidam Basin

ABSTRACT

The discovery of natural gas trapped in the late Neogene Shizigou Formation in the Yikeyawuru anticline indicates the potential for additional microbial gas reservoirs outside of the primary exploration targets for microbial gas in the younger, i.e., the Pleistocene sediments of the Qaidam Basin. In this study, a detailed investigation is presented on the bulk geochemistry and organic petrography of the potential microbial source rocks as well as on molecular organic geochemistry of the solvent extracts obtained from the late Neogene Shizigou Formation of the Yiliping Depression. The objectives are to elucidate i) the depositional environment, ii) biological sources of organic matter (OM), and iii) biodegradation levels in these microbial gas source rocks.

The samples from the well situated at the center of the Yiliping Depression (the H 1 well) exhibit minor variations in total organic carbon (TOC) and total sulfur contents, whereas the samples from the well located at the margin of the depression (the Y 3 well) show large variations in these values. All these samples are presently thermally immature. The kerogen of the TOC-rich Y 3 well samples is mainly composed of mixed types II–III kerogen and characterized by a complex maceral composition (i.e., a mixture of large fragments of huminite, semifusinite, fusinite, resinite/fluorinite, lamalginite, and liptodetrinite). In contrast, samples from the H 1 well contain typically type III kerogen with a less complex maceral composition consisting of huminite, lamalginite, and liptodetrinite. The molecular data illustrates that the OM is predominantly derived from bacterial and algal biomass as well as aquatic higher plants (primarily in the Y 3 well samples), while angiosperms are the primary source of the subordinate terrestrial OM in the samples. The marginal area is characterized by salinity levels akin to normal marine conditions with bottom-water paleoredox conditions ranging from dyoxic (samples with high TOC content) to oxic, whereas the central area developed a mesosaline environment with oxic bottom-water conditions prevailing. In contrast to the primary microbial gas producing layer, the Pleistocene Qigequan Formation, the late Neogene Shizigou Formation exhibits a higher contribution of emergent macrophytes but a reduced abundance of lower aquatic organisms in the OM as well as a higher salinity level in the water column. Despite the late Neogene Shizigou Formation demonstrating a lower potential for hydrocarbon generation and a lower degree of biodegradation of OM than the Qigequan Formation, it still shows generally favorable geological and geochemical conditions that are conducive to the development of microbial gas reservoirs, which is underscored by the biodegradation levels between 3 and 4 for the studied samples.

* Corresponding author at: Basin and Reservoir Research Center, China University of Petroleum, No. 18, Fuxue Road, Changping District, Beijing, China.
E-mail addresses: jinqi.qiao@cup.edu.cn (J. Qiao), qingyong.luo@cup.edu.cn (Q. Luo), ralf.littke@emr.rwth-aachen.de (R. Littke).

https://doi.org/10.1016/j.coal.2024.104658
Received 25 September 2024; Received in revised form 14 November 2024; Accepted 15 November 2024
Available online 19 November 2024

1. Introduction

While marine source rocks contribute most to the Earth's petroleum resources, lacustrine source rocks play also a significant role in the global carbon cycle and generate a considerable volume of hydrocarbons (e.g., Demaison and Huizinga, 1991; Carroll and Wartes, 2003; Qiao et al., 2023). Furthermore, some of the most organic matter (OM) rich sedimentary units in terms of total organic carbon (TOC) content and thickness are of lacustrine origin (Demaison and Huizinga, 1991; Carroll and Wartes, 2003). However, lacustrine settings present greater complexity compared to marine settings attributable to the diverse origins of OM and variations in water environments (e.g., salinity and redox conditions) (Scott et al., 2012; Goodarzi, 2020a). Notably, alkaline lacustrine sediments have attracted increasing attention due to their distinctive features, such as high hydrocarbon generation potential, high organic sulfur content, and lower thermal maturity for the onset of hydrocarbon generation compared to sediments from freshwater lacustrine settings (e.g., Rippen et al., 2013; Luo et al., 2018; Cichon-Pupienis et al., 2021; Qiao et al., 2023; Xiao et al., 2024). Of particular significance is the largest commercial Quaternary accumulation of microbial gas worldwide, which is generated and trapped in saline-hypersaline sediments in the Qaidam Basin in China (Qiao et al., 2021a and 2022). Microbial gas is typically generated by the bio-degradation of OM in sediments at low temperatures (up to 75 °C), but the optimum seems to be about 35–50 °C (Rice and Claypool, 1981; Katz, 2011). The burial depth at which microbial gas is generated is affected by various sedimentological and physicochemical conditions (e.g., nutrient supply, availability of degradable OM). Generally, the greatest proportion of microbial gas production occurs at depths of about 1 km and the deepest microbial gas has been documented occurring as deep as 3.35 km (Rice and Claypool, 1981). These conditions required for the formation of microbial gas mean that its reservoirs are limited with respect to their depth range. Future exploration efforts may be focused on strata with similar burial depths to the Qigequan Formation to discover more microbial gas reservoirs.

In the Qaidam Basin, a large alkaline paleo-lake developed during the Neogene and Pleistocene epochs in which extensive alkaline lacustrine sediments were deposited (Song et al., 2022). The primary focus of microbial gas exploration lies within the Pleistocene Qigequan Formation, renowned for its considerable thickness (the maximum thickness exceeding 2 km; Fig. 1c and d) (e.g., Pang et al., 2005; Qiao et al., 2021a). However, the depth constraint for the occurrence of microbial gas in the Qaidam Basin is not yet known. Additionally, the potential existence of large microbial gas fields in the late Neogene Shizigou Formation, which underlies the Qigequan Formation warrants further investigation. The late Neogene Shizigou Formation is buried too deeply in the main producing area of the Qigequan Formation, the Sanhu Depression, making it unfavorable for the generation of microbial gas (Qiao et al., 2021a; Fig. 1c and d). However, in the western Qaidam Basin, the Shizigou Formation is buried at a shallower depth (shallower than 2 km; Fig. 1c and d), offering a promising new prospect for gas exploration in the basin.

It is an important objective to expand microbial gas exploration in the Qaidam Basin by assessing whether the late Neogene Shizigou Formation possesses the requisite conditions for microbial gas generation. In comparison to the margins of the basin where the lithology is mainly

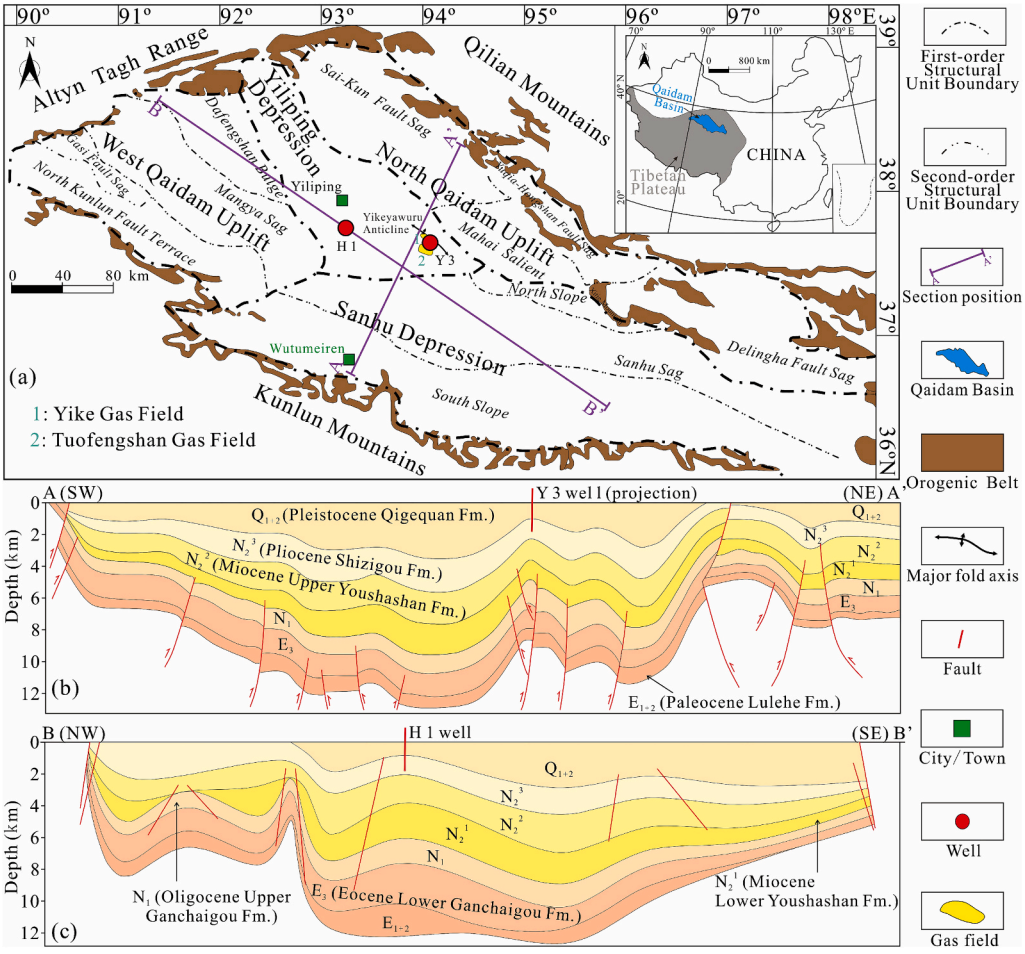

Fig. 1. (a) Schematic map showing the location of the Qaidam Basin in China, (b) its geological setting and sample well locations, as well as (c) SW-NE (modified after Zhou et al., 2006) and (d) NW-SE (modified after Qiu et al., 2003) transects. Note: The stratigraphic information in c and d is shown more accurately in Fig. 2.

composed of sandstone, glutenite, and conglomerate, the Yiliping Depression, situated at the depocenter of the Shizigou Formation (as shown in Fig. 1a), is deemed to be more conducive to the generation and accumulation of microbial gas based on the core lithology (Fig. 2) (Song et al., 2022). In the Yiliping Depression, the evidence of active methanobacteria in the late Neogene Shizigou Formation within the H 1 well (Liu et al., 2011), as well as the discovery of trapped microbial gas in the late Neogene Shizigou Formation of the Yikeyawuru anticline near the Y 3 well (shown in Fig. 1a), strongly suggest that the exploration target for microbial gas could potentially be expanded to the late Neogene Shizigou Formation. However, one fundamental issue that arises in exploring the Shizigou sediments lies in the lack of any detailed geochemical characterization compared to the Pleistocene exploration system.

Thus, this investigation focuses on interpreting new elemental analysis, programmed open-system pyrolysis, as well as molecular organic geochemical, and petrographic data on the Shizigou sediments, which were sampled from the H 1 and Y 3 wells in the Yiliping Depression. The goal is to furnish comprehensive information on the quality and quantity of OM, depositional environment, kerogen type, and the related evidence of microbial gas generation. Such insights are crucial for identifying potential areas conducive to microbial gas discovery and subsequent exploration efforts.

2. Geological setting

The Qaidam Basin is a rhomb-shaped intermontane basin, encompassing an area of approximately 12×10^4 km^2 (Jian et al., 2013). It is also the largest basin in the Qinghai-Tibetan Plateau, with altitudes ranging from 2.7 to 3.5 km above sea level (Jian et al., 2013). Since the Oligocene epoch, the Qaidam Basin has predominantly existed as an intermontane basin within a relatively enclosed system, delineated from the surrounding mountain ranges with elevations ranging from 4 to over 5 km by large-scale faults (Pang et al., 2005; Jian et al., 2013). These encompass the Eastern Kunlun Mountains to the southwest (SW), the Qilian Mountains to the northeast (NE), and the Altyn Tagh Range to the northwest (NW) (Fig. 1a; Tapponnier et al., 2001; Qiao et al., 2021a and 2022).

The formation of the basin, situated at the northeastern edge of the plateau, ensued from the convergent dynamics of the plateau (Tapponnier et al., 2001). The Mesozoic tectonic evolution of the basin was influenced by the movements and collisions of the Meso-Tethys, Neo-Tethys and Mongol-Okhotsk Ocean blocks (Gehrels et al., 2011). Throughout the Cenozoic era, the tectonic evolution of the basin was shaped by the Qinghai-Tibetan Plateau elevation and the collision between the Indian and Eurasian plates (Harrison et al., 1992; Tapponnier et al., 2001; Royden et al., 2008). A Mesozoic-Cenozoic sedimentary succession, ranging in thickness from 3 to 16 km, was developed above the basement comprising pre-Mesozoic metamorphic and igneous rocks. In certain regions, the Cenozoic sediments attain a maximum thickness of 12 km (Fig. 1b and c) (Pang et al., 2005; Jian et al., 2013). The Qaidam Basin developed terrestrial coal-bearing strata during the Jurassic epoch (Huang et al., 2022; Wu et al., 2022; Liu et al., 2023a). Since the Eocene epoch, the sediments were deposited under fluvial and lake facies and almost continuously penetrated most areas of the basin, primarily derived from the surrounding mountains (Heermance et al., 2013).

The Qaidam Basin consists of four primary structural units, namely the North Qaidam Uplift, the Yiliping Depression, and the West Qaidam Uplift from east to west in the north part as well as the Sanhu Depression in the south of the basin (Fig. 1a). The Yiliping Depression spans an area of approximately 7.3×10^4 km^2. Most anticlines, such as the Yikeyawuru Anticline, exhibit a NW-SE (southeast) orientation due to the joint action of the Altun Mountains left-lateral strike-slip fault and the Qilian Mountains fold-thrust (Gong et al., 2023). The late Neogene Shizigou Formation in the Yiliping Depression is composed of mudstone, sandy mudstone, and argillaceous siltstone, as well as occasional black argillaceous limestone (Fig. 2).

3. Samples and methods

3.1. Sample preparation

In this study, a total of 68 samples of the late Neogene Shizigou Formation were gathered from two wells. Among them, nine samples were obtained from the H 1 well with depths ranging from 1507 to 1919 m and 59 samples from the Y 3 well with depths ranging from 1106 to 1390 m. Each sample was divided into two aliquots. The first part was pulverized into a fine powder using a disc mill, with analysis of elemental composition and programmed open-system pyrolysis performed on particles smaller than 120 mesh, and solvent extraction on particles smaller than 80 mesh. The second aliquot was prepared as a polished section for microscopic investigations. The polished sections are basically prepared following the international standard "Methods for the petrographic analysis of coals – Part 2: methods of preparing coal samples" (ISO 7404-2, 2009), which was originally established for the preparation of coal samples. First, rock pieces were cut perpendicular to the bedding with a size of approximately 3–5 cm^2. Second, the rock pieces were placed into molds and epoxy resin was slowly poured around them. Third, the samples were left at room temperature for a few days until the bubbles disappeared, and the epoxy hardened. Fourth the samples were buffed using 300-, 600-, and 1200-grit sandpaper in sequence, followed by sequentially polishing with aluminium oxide and 0.05 μm polishing liquid using a polisher cloth (EcoMet 250-AutoMet 250). Finally, the sections were washed with deionized water and air-dried for use.

3.2. Elemental analysis

The TOC and total sulfur (TS) contents were measured using a Leco CS-230 (USA). Prior to measurement, the aliquots were digested with a mixed solvent of hydrochloric acid (HCl) and deionized water (in a 1:7 ratio by volume) at a temperature below 80 °C for a minimum of 2 h to remove carbonates. The treated samples were then washed with deionized water to neutralize the pH. Approximately 1.0 g of the dried powders were used for the measurements by recording the amounts of CO_2 and SO_2, using a non-dispersive infrared detector.

3.3. Programmed open-system pyrolysis

Programmed open-system pyrolysis was conducted using a Wildcat Technologies Hydrocarbon Analyzer workstation (HAWK) (Houston, USA). Approximately 50 mg were placed in the autosampler tray of the instrument.

The pyrolysis was carried out in an inert nitrogen atmosphere, with an isothermal temperature set at 300 °C for 3 min to release the S_1 fraction (quantity of free and sorbed hydrocarbon, mg HC/g rock), which is followed by a ramp stage of heating the oven to 650 °C at a rate of 25° per minute to measure the S_2 fraction (generated hydrocarbon, mg HC/g rock). The S_3 fraction (oxygen-containing organic carbon released from kerogen thermal breakdown, mg CO_2/g rock) is also recorded by measuring the amount of CO_2.

Before the first sample and after every 20 samples, one standard and one blank sample were measured.

3.4. Organic petrography

The maceral group "vitrinite" only occurs from the bituminous coal stage onward strictly speaking, as its glass-like appearance (derived from the Greek word "vitros," meaning glass) is not present at lower thermal maturities. Therefore, coal petrologists prefer to use the term "huminite" for earlier diagenetic stages. However, in geology and the petroleum industry—where vitrinite reflectance is commonly

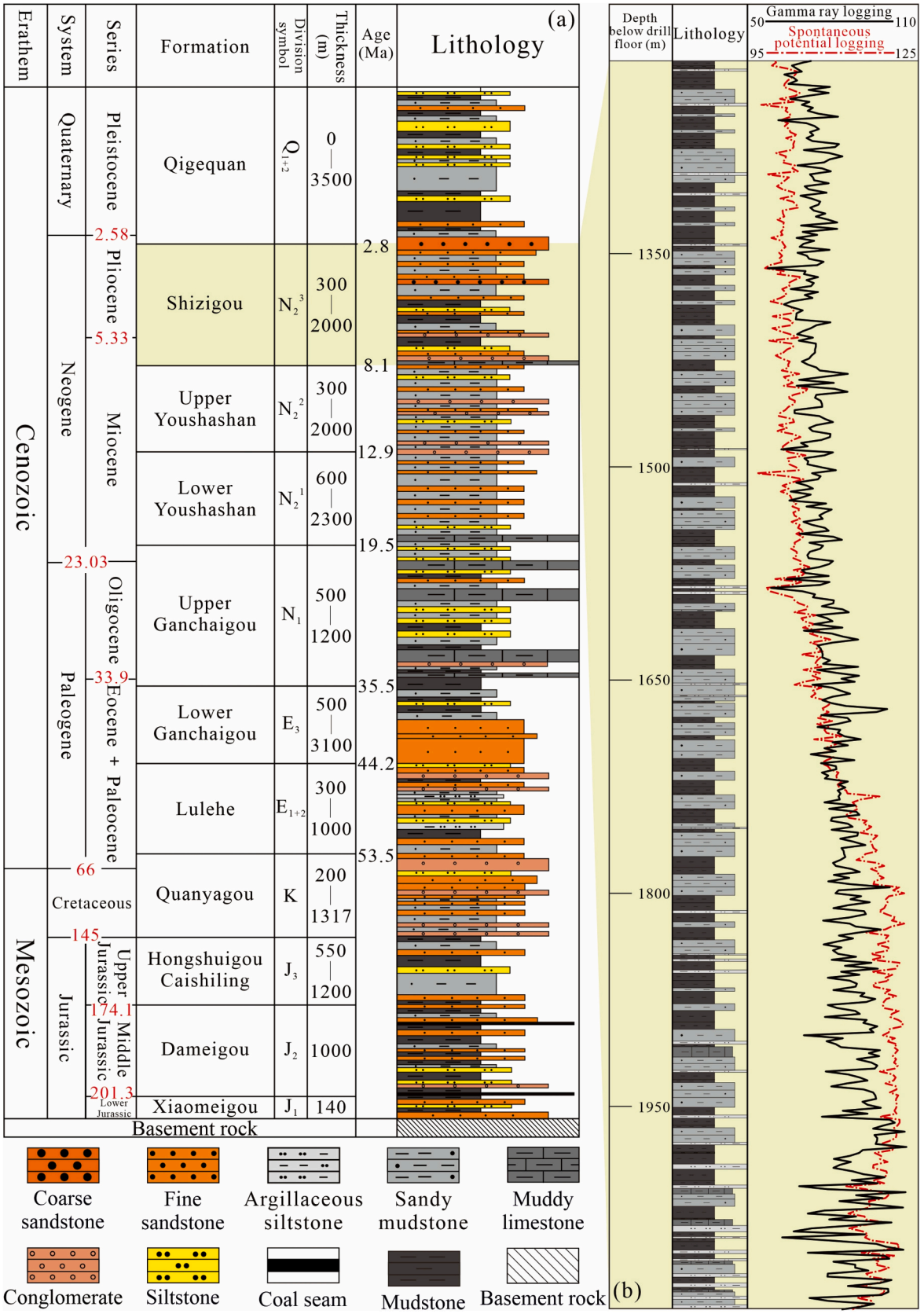

Fig. 2. (a) Generalized stratigraphic column for the Qaidam Basin and (b) the detailed stratigraphic column in the H 1 well.

utilized—the term "huminite" is less recognized. Actually, the vitrinite and huminite systems have been correlated, allowing the two systems to be used in parallel down to the level of sub-maceral groups (Sýkorová et al., 2005). To avoid confusion, we use "huminite" when referring to the maceral group, and "huminite/vitrinite reflectance (VR_r)" when discussing reflectance. A Leica DM4500P microscope (Germany) equipped with a CRAIC microscope photometer, which is operated with DISKUS Fossil software (Hilgers) both in reflected white light (halogen) and in an ultraviolet (UV) fluorescence irradiation at a magnification of 500 × (50 × oil immersion objective) was utilized to determine maceral composition and measure VR_r. A filter BV-2A (EX 420/40; DM 455; BA 460) was used for fluorescence microscopy. Reflected and fluorescence light modes were used to observe macerals of inertinite and huminite as well as liptinite groups, respectively. The VR_r was measured using a microscope photometer (MPV-SP) at a wavelength of 546 nm with at least 50 randomly oriented huminite particles measured for each sample whenever possible, according to ISO 7404–5:, 2009. The equipment was calibrated before each measurement with a standard of known reflectance (LEUKO–SAPHIR, 0.589%). The classification and identification of macerals followed the nomenclature of the ICCP system (ICCP, 1998; ICCP, 2001; ISO 7404-3, 2009; Pickel et al., 2017; Gonçalves et al., 2024).

3.5. Molecular analysis

3.5.1. Extraction and fractionation

In this study, a Soxhlet extractor was used to extract bitumen due to rather low TOC contents in the studied samples. Approximately 80–120 g of powdered samples were extracted based on the S_1 values in the samples. The extraction was performed using dichloromethane (DCM) and the removal of elemental sulfur was achieved by adding copper powder to the extracts.

The extracts were separated into four fractions. Asphaltene was precipitated via a settlement of the extracts solved with *n*-hexane for over 12 h. The remaining three fractions including aliphatic hydrocarbons, aromatic hydrocarbons and NSO (nitrogen-, sulfur-, and oxygen-containing) components were washed with eluents of different polarity including *n*-hexane (30 mL), a mixed solvent of *n*-hexane/DCM (20 mL), and anhydrous ethanol (10 mL) followed by trichloromethane (10 mL) in turn via column chromatography.

3.5.2. GC–MS analyses

The analyses of aliphatic and aromatic hydrocarbon fractions were performed by gas chromatography (GC)-mass spectrometry (MS) on an Agilent 6890 (GC) linked to a 5975i mass selective detector (MS) and an Agilent 7890B (GC) linked to a 5977A (MS), respectively. Carrier gas used was helium with a velocity of 1 mL/min.

The MS conditions are the same for the analyses of aliphatic and aromatic hydrocarbon fractions. The MS was operated in electron ionization (EI+) mode with an ionization energy of 70 eV and a source temperature of 230 °C in full scan mode. HP-5MS fused silica capillary columns of 30 m and 60 m in length with 0.25 mm ID (inner diameter) were used. The GC conditions for analyses of both hydrocarbon fractions were set to 300 °C injector temperature with 1 μL spitless injections.

The GC oven temperature used for analyzing aliphatic hydrocarbon fractions was initially set at 50 °C with an isothermal hold time of 1 min. Subsequently, the temperature was ramped up to 100 °C at a rate of 20 °C/min, followed by a further increase to 310 °C at a rate of 3 °C/min, with a final hold time of 10 min. The GC oven temperature used for analyzing aromatic hydrocarbon fractions was set at 80 °C with an isothermal hold time of 1 min. This was followed by a ramp up to 310 °C at a rate of 3 °C/min, with a final hold time of 25 min.

The calculated biomarker parameters in question were established on the basis of the peak areas of specific ion chromatograms. The identification of each compound was carried out through a meticulous comparison of elution sequences in comparison to published literature (e.g., Luo et al., 2018; Grohmann et al., 2019; Zheng et al., 2022; Wu et al., 2023).

4. Results

4.1. Elemental composition

TOC contents in the samples obtained from the Y 3 well range between 0.02 and 7.35% with an average value of 0.64% and TS contents between 0.00 and 6.35%, averaging at 0.50%. In contrast, both TOC and TS contents measured in the samples from the H 1 well show little variation with TOC contents of 0.25–0.35% (avg. 0.29%) and TS contents of 0.23–1.10% (0.57% on average). The TOC/TS ratios for the Y 3 well and H 1 well are 0.08–16.57 (3.26 on average) and 0.24–1.22 (avg. 0.70), respectively (Table 1).

4.2. Programmed open-system pyrolysis

The results of programmed open-system pyrolysis are presented in Table 1. For the samples from the H 1 well, S_1 and S_2 values are 0.03–0.07 (0.05 on average) and 0.13–0.17 (0.15 on average) mg HC/g rock, respectively. The values of these two parameters are similar to the Pleistocene samples from the same well (Qiao et al., 2021a). S_3 values vary from 0.26 to 0.42 mg CO_2/g rock with an average value of 0.36 mg CO_2/g rock. Hydrogen index (HI = S_2/TOC) and oxygen index (OI = S_3/TOC) values are 42–64 (avg. 53) mg HC/g TOC and 99–171 (avg. 127) mg CO_2/g TOC, respectively. The programmed open-system pyrolysis data for the Y 3 well exhibit larger variation in comparison to the data of the H 1 well. For the samples from the Y 3 well, S_1 and S_2 values are 0.03–0.76 (avg. 0.09 mg HC/g rock) and 0.04–9.08 (avg. 0.80 mg HC/g rock), respectively. S_3 values range from 0.22 to 2.08 (0.55 mg CO_2/g rock on average). HI value varies between 20 and 209 mg HC/g TOC (90 mg HC/g TOC on average) and OI between 18 and 1792 mg CO_2/g TOC (avg. 360 mg CO_2/g TOC). T_{max} (temperature of maximum pyrolysis yield) values vary in the samples from the H 1 well ranging between 393 and 439 °C (424 °C on average). In contrast, the samples from the Y 3 well show minor variations in T_{max}, ranging from 408 to 421 °C, with an average of 415 °C.

4.3. Organic petrography

A small number of the samples with high TOC content (1.65–7.35%) from the Y 3 well, such as Y3–18, Y3–27, Y3–36 and Y3–44, exhibit numerous autochthonous huminite particles. The huminite particles show a dark-grey color, particularly ulminite (Fig. 3a, b, and g), with varying shapes observed (Fig. 3a-c). These huminite particles can be observed as i) massive huminite mixed with resinite (Fig. 3f and g), ii) massive and homogeneous huminite (Fig. 3 a, b, and c). By contrast, the samples with low TOC content show detrital huminite with areas smaller than 50 μm^2 (Fig. 3d and e). The VR_r values measured range between 0.18 and 0.39% with standard deviations ranging between 0.03 and 0.08 (Table 1). Considering the range of the VR_r and low fluorescence intensity in ulminite (Fig. 3g), ulminite can be further classified as ulminite B, partly grading into bituminite. Moreover, large semifusinite (Fig. 3b) and fusinite (Fig. 3c), two types of inertinite maceral group, can be observed in some samples with high TOC content. In the case of samples with high TOC content from the Y 3 well, liptinite appears mainly as resinite (Fig. 3f-h) and sporinite (Fig. 3h) with very rare telalginite and liptodetrinite (Fig. 3g and h). Comparatively, liptinite composition in the samples from the H 1 well and samples from the Y 3 well with low TOC content is simple and primarily composed of liptodetrinite and planar lamalginites (Fig. 3i). Pyrite is abundant in the samples with high TOC content from the Y 3 well, occurring as assemblages of framboidal pyrites or euhedral crystals (Fig. 3a, b, and c). In the samples with low TOC content, only euhedral crystal pyrite can be observed with rare abundance (Fig. 3d and e). It should be emphasized

Table 1
Measured results of TOC content (wt%), TS content (wt%) and programmed open-system pyrolysis for the sediments from the Shizigou Formation in the Yiliping Depression, Qaidam Basin, China. $\bar{x}$ = average value, Std = standard deviation, n = number of VR_r measured.

Well	Sample ID	Depth (m)	TOC (wt%)	TS (wt%)	VR_r (%)			Programmed open-system pyrolysis data							
					$\bar{x}$	Std.	n	T_{max} (°C)	S_1 (mg HC/g rock)	S_2 (mg HC/g rock)	S_3 (mg CO_2/g rock)	HI (mg HC/g TOC/g)	OI (mg CO_2/g TOC)	$(S_1 + S_2)$/TOC	S_2/S_3
Y 3	Y3–1	1106.20	0.22	0.04	n.d.	n.d.	n.d.	429	0.06	0.12	0.84	56	391	0.82	0.14
	Y3–4	1110.20	0.05	0.00	n.d.	n.d.	n.d.	411	0.04	0.04	0.70	82	1429	1.60	0.06
	Y3–5	1113.50	0.28	0.38	0.21	0.04	51	427	0.06	0.35	0.63	125	226	1.46	0.56
	Y3–6	1114.60	0.10	0.05	n.d.	n.d.	n.d.	432	0.03	0.09	0.75	90	750	1.20	0.12
	Y3–7	1116.74	0.06	0.00	n.d.	n.d.	n.d.	439	0.03	0.07	0.32	121	552	1.67	0.22
	Y3–8	1118.90	0.05	0.01	n.d.	n.d.	n.d.	426	0.04	0.07	0.42	152	913	2.20	0.17
	Y3–10	1121.55	0.08	0.01	n.d.	n.d.	n.d.	427	0.03	0.06	0.48	72	578	1.13	0.13
	Y3–18-917	1122.60	0.98	1.23	n.d.	n.d.	n.d.	432	0.09	1.35	0.44	138	45	1.47	3.07
	Y3–11	1122.60	0.11	1.33	n.d.	n.d.	n.d.	417	0.03	0.08	0.54	72	486	1.00	0.15
	Y3–12	1124.80	0.16	1.00	n.d.	n.d.	n.d.	414	0.06	0.13	0.50	82	314	1.19	0.26
	Y3–13	1125.50	0.24	0.41	n.d.	n.d.	n.d.	428	0.05	0.19	0.86	78	354	1.00	0.22
	Y3–18-918	1126.10	0.31	0.16	n.d.	n.d.	n.d.	429	0.05	0.17	0.41	55	133	0.71	0.41
	Y3–14	1126.70	0.08	0.28	n.d.	n.d.	n.d.	412	0.03	0.08	0.59	98	720	1.38	0.14
	Y3–15	1127.63	0.04	0.18	n.d.	n.d.	n.d.	416	0.03	0.06	0.61	143	1452	2.25	0.10
	Y3–16	1129.00	0.34	0.33	n.d.	n.d.	n.d.	431	0.05	0.35	0.60	102	175	1.18	0.58
	Y3–17	1130.30	0.04	0.00	n.d.	n.d.	n.d.	426	0.03	0.04	0.41	105	1079	1.75	0.10
	Y3–18	1131.72	1.65	1.13	0.28	0.07	56	429	0.13	2.95	0.94	179	57	1.87	3.14
	Y3–19	1131.80	3.79	6.35	0.29	0.03	68	428	0.19	6.22	1.84	164	49	1.69	3.38
	Y3–20	1132.00	0.32	1.01	n.d.	n.d.	n.d.	417	0.05	0.24	0.65	74	201	0.91	0.37
	Y3–21	1132.95	0.02	0.15	n.d.	n.d.	n.d.	422	0.03	0.05	0.43	208	1792	4.00	0.12
	Y3–22	1134.66	0.04	0.08	n.d.	n.d.	n.d.	393	0.04	0.06	0.47	143	1119	2.50	0.13
	Y3–23	1360.15	0.07	0.44	n.d.	n.d.	n.d.	422	0.03	0.05	0.59	68	797	1.14	0.08
	Y3–24	1361.40	0.24	0.42	n.d.	n.d.	n.d.	421	0.03	0.05	0.66	20	270	0.33	0.08
	Y3–25	1362.60	0.02	0.01	n.d.	n.d.	n.d.	413	0.05	0.04	0.25	167	1042	4.50	0.16
	Y3–26	1363.50	0.99	0.24	n.d.	n.d.	n.d.	429	0.06	0.58	0.48	59	49	0.65	1.21
	Y3–27	1364.68	1.31	0.55	0.39	0.04	53	423	0.09	0.56	0.87	43	66	0.50	0.64
	Y3–28	1365.00	0.07	0.39	n.d.	n.d.	n.d.	416	0.04	0.05	0.82	74	1206	1.29	0.06
	Y3–29	1365.10	0.35	0.05	n.d.	n.d.	n.d.	428	0.09	0.27	0.47	78	136	1.03	0.57
	Y3–30	1366.40	0.09	0.01	n.d.	n.d.	n.d.	437	0.05	0.08	0.55	92	632	1.44	0.15
	Y3–31	1367.00	0.25	0.35	n.d.	n.d.	n.d.	429	0.03	0.19	0.38	76	152	0.88	0.50
	Y3–32	1367.50	0.28	0.74	n.d.	n.d.	n.d.	428	0.04	0.20	0.39	72	141	0.86	0.51
	Y3–33	1368.40	0.29	0.30	n.d.	n.d.	n.d.	415	0.05	0.16	0.48	55	166	0.72	0.33
	Y3–34	1368.72	0.22	0.15	n.d.	n.d.	n.d.	415	0.08	0.09	0.47	40	211	0.77	0.19
	Y3–35	1369.90	0.28	0.62	n.d.	n.d.	n.d.	418	0.08	0.13	0.36	47	131	0.75	0.36
	Y3–36	1370.95	3.03	1.81	0.22	0.08	65	427	0.42	6.33	0.56	209	18	2.23	11.30
	Y3–37	1371.50	0.24	0.45	n.d.	n.d.	n.d.	408	0.10	0.11	0.27	46	112	0.88	0.41
	Y3–38	1373.95	0.18	0.00	n.d.	n.d.	n.d.	438	0.06	0.05	0.45	29	257	0.61	0.11
	Y3–39	1374.50	0.36	0.03	n.d.	n.d.	n.d.	435	0.10	0.38	0.27	105	75	1.33	1.41
	Y3–40	1374.98	0.23	0.03	n.d.	n.d.	n.d.	432	0.08	0.14	0.30	61	131	0.96	0.47
	Y3–41	1375.40	0.19	0.03	n.d.	n.d.	n.d.	432	0.07	0.09	0.32	47	166	0.84	0.28
	Y3–42	1376.50	0.57	0.55	n.d.	n.d.	n.d.	430	0.09	0.62	0.38	110	67	1.25	1.63
	Y3–43	1377.45	0.67	0.70	n.d.	n.d.	n.d.	423	0.18	0.82	0.35	122	52	1.49	2.34
	Y3–44	1377.95	4.35	2.11	0.18	0.04	75	410	0.42	4.88	0.79	112	18	1.22	6.18
	Y3–45	1378.50	2.20	1.01	0.20	0.03	57	417	0.16	2.33	0.49	106	22	1.13	4.76
	Y3–46	1379.95	0.20	0.00	n.d.	n.d.	n.d.	432	0.07	0.07	0.42	34	207	0.70	0.17
	Y3–47	1380.20	0.26	0.06	n.d.	n.d.	n.d.	429	0.13	0.14	0.24	54	93	1.04	0.58
	Y3–48	1380.50	7.35	2.44	0.23	0.03	62	415	0.76	9.08	2.08	124	28	1.34	4.37
	Y3–49	1381.25	0.47	0.05	n.d.	n.d.	n.d.	430	0.06	0.14	0.38	30	81	0.43	0.37
	Y3–50	1382.50	0.18	0.04	n.d.	n.d.	n.d.	422	0.05	0.06	0.22	34	124	0.61	0.27
	Y3–51	1383.50	0.22	0.04	n.d.	n.d.	n.d.	432	0.04	0.08	0.40	36	180	0.55	0.20
	Y3–52	1384.60	0.23	0.05	n.d.	n.d.	n.d.	431	0.09	0.09	0.39	39	170	0.78	0.23
	Y3–53	1385.10	1.16	0.07	0.37	0.05	54	434	0.09	1.55	0.48	134	41	1.41	3.23

(*continued on next page*)

Table 1 (*continued*)

Well	Sample ID	Depth (m)	TOC (wt%)	TS (wt%)	VR_r (%)			Programmed open-system pyrolysis data							
					$\bar{x}$	Std.	n	T_{max} (°C)	S_1 (mg HC/g rock)	S_2 (mg HC/g rock)	S_3 (mg CO_2/g rock)	HI (mg HC/g TOC/g)	OI (mg CO_2/g TOC)	$(S_1 + S_2)$/TOC	S_2/S_3
H 1	Y3–54	1386.45	0.90	0.07	n.d.	n.d.	n.d.	434	0.10	1.77	0.31	197	35	2.08	5.71
	Y3–55	1387.35	0.96	1.36	n.d.	n.d.	n.d.	424	0.07	1.02	0.50	106	52	1.14	2.04
	Y3–56	1388.85	0.20	0.03	n.d.	n.d.	n.d.	416	0.04	0.06	0.40	30	198	0.50	0.15
	Y3–57	1389.90	0.15	0.03	n.d.	n.d.	n.d.	423	0.05	0.04	0.33	26	217	0.60	0.12
	18–905	1507.70	0.28	0.23	n.d.	n.d.	n.d.	421	0.05	0.15	0.38	54	136	0.71	0.39
	18–906	1512.30	0.27	0.87	n.d.	n.d.	n.d.	408	0.05	0.13	0.41	48	152	0.67	0.32
	18–907	1518.00	0.26	0.29	n.d.	n.d.	n.d.	413	0.05	0.14	0.26	54	100	0.73	0.54
	18–908	1519.40	0.30	0.51	0.23	0.03	51	419	0.05	0.17	0.40	57	134	0.73	0.43
	18–909	1526.50	0.25	0.25	n.d.	n.d.	n.d.	421	0.03	0.14	0.42	57	171	0.68	0.33
	18–910	1529.90	0.30	1.10	n.d.	n.d.	n.d.	410	0.07	0.17	0.35	57	118	0.80	0.49
	18–911	1905.30	0.26	1.09	n.d.	n.d.	n.d.	417	0.07	0.17	0.31	64	117	0.92	0.55
	18–912	1911.20	0.35	0.29	0.21	0.06	52	415	0.05	0.16	0.34	46	99	0.60	0.47
	18–913	1915.30	0.31	0.53	n.d.	n.d.	n.d.	412	0.05	0.13	0.35	42	112	0.58	0.37

that the presence of framboidal pyrites within or near huminite (Fig. 3a, b, c) indicates that organic material is autochthonous because this pyrite-huminite association does commonly not appear in re-worked or re-deposited organic material due to rapid pyrite oxidation under weathering or surface conditions (Littke et al., 1991; Nzoussi-Mbassani et al., 2005). The physical characteristics of huminite macerals, such as being angular and massive, also suggest they are primary. Although massive and angular huminite, as well as huminite associated with framboidal pyrite, are difficult to observe in the samples with low TOC content, the VR_r values in these low TOC samples are similar to those from the samples with high TOC content. Furthermore, the low VR_r values and low standard deviations across all measured samples suggest that these phytoclasts are primary (Synnott et al., 2017).

4.4. Molecular composition

4.4.1. *n*-Alkanes, acyclic isoprenoids, and bicyclic alkanes

The chromatograms of the investigated samples show that the normal alkanes (*n*-alkanes) constitute the major compounds, ranging from *n*-C_8 to *n*-C_{31}, with a bimodal distribution exhibiting maxima at *n*-C_{16}, or *n*-C_{18} for the short-chain homologs (<*n*-C_{21}) and at *n*-C_{25}, *n*-C_{27} or *n*-C_{29} for the middle- and long-chain homologs (>*n*-C_{20}) in most samples (Fig. 4a and b; Table 2). The distribution characteristics of short-chain *n*-alkanes are very similar with $CPI_{12–20}$ values ranging from 0.63 to 1.60 and with an average value of 0.81 (Table 2). Of particular interest is the fact that the distribution characteristics of middle and long-chain *n*-alkanes from the Y 3 well, especially the samples with high TOC content, exhibit a marked deviation from those of the H 1 well. For the samples from the Y 3 well, there is a clear preference of odd *n*-alkanes in the middle- and long-chains with the carbon preference index ($CPI_{24–34}$) (Bray and Evans, 1961) ranging between 1.44 and 5.94 (3.79 on average) (Table 2). Moreover, the TAR (terrigenous/aquatic ratio) (Bourbonniere and Meyers, 1996) ranges from 0.61 to 6.59 (avg. 2.18), *n*-C_{17}/*n*-C_{27} ratios from 0.14 to 4.27 (avg. 1.35) and Paq (submerged/floating macrophytes) (Ficken et al., 2000) ratios from 0.18 to 0.68 (0.43 on average). Average chain length (ACL) is 26.15–28.95 (avg. 27.61) (Fig. 4a and b) (Table 2). For the samples from the H 1 well, the odd-even predominance is not apparent with the $CPI_{24–34}$, TAR, *n*-C_{17}/*n*-C_{27} ratios, Paq and ACL being 1.29–1.83 (avg. 1.02), 0.46–3.43 (avg. 1.32), 0.82–6.22 (2.45), 0.39–0.65 (avg. 0.56), and 26.46–28.30 (avg. 27.14), respectively (Table 2). Moreover, large variations in concentrations of β-carotane (*m/z* 125) can be observed with β-carotane/*n*-C_{25} ranging between 0.01 and 2.57 (0.32 on average) (Table 2).

By contrast, the distribution characteristics of acyclic isoprenoids from the two wells are similar. Pristane (Pr) or phytane (Ph) are the most abundant acyclic isoprenoids, with Pr/Ph ratio of 0.26–1.19 with an average value of 0.80 (Table 2). The relative abundances of Pr and Ph in comparison to their adjacent *n*-alkanes (i.e., Pr/*n*-C_{17} and Ph/*n*-C_{18}) are 0.60–1.62 and 0.59–6.30, respectively (Table 2). The C_{30} isoprenoid (squalane) and C_{25} isoprenoid (PMI) are also observed with PMI/*n*-C_{26} varying from 0.12 to 2.69 (0.74 on average) and squalene/*n*-C_{22} from 0.12 to 0.70 (avg. 0.33). Moreover, the bicyclic alkanes 8β-(H)-drimane (D) and 8β-(H)-homodrimane (HD) are observed in the *m/z* 123 mass chromatogram with the ratios of HD/D being 1.81–38.36 (10.67 on average; Table 2). However, diterpenoids' abundances are below the detection limit in most cases.

4.4.2. Terpanes

Terpanes can be observed in the *m/z* 191 mass chromatogram. Tricyclic terpanes (Tri) ranging from C_{19} to C_{29}, with the exception of C_{28}, are identified in all samples (Fig. 4c and d). In the short chains of Tri, increasing trends can be observed from C_{19} to C_{21} Tri, while decreasing trends are shown in Tri from C_{23} to C_{25}. Besides, the contents of C_{22} Tri are similar to those of C_{21} and C_{25} Tri.

Extended Tri (C_{28} and C_{29}) exhibit a wide range of variation in the (C_{28} Tri + C_{29} Tri)/Ts ratio (ETR) (Holba et al., 2001), with values

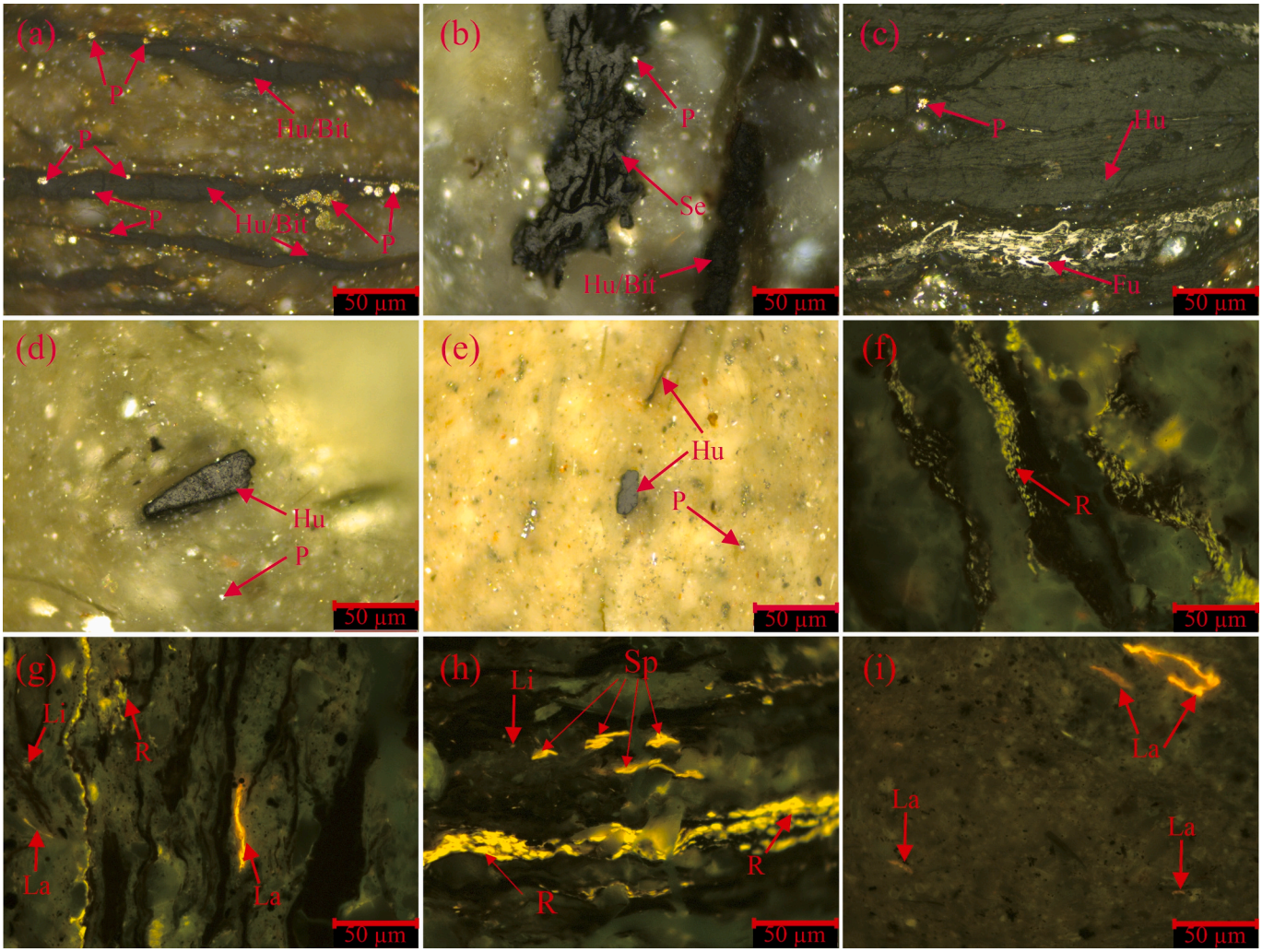

Fig. 3. Microphotographs showing macerals in the Pliocene source rocks under incident reflected white light (a-e) and in fluorescence mode (f-i). a: sample Y3–36; b: sample Y3–27; c: sample Y3–44; d: sample Y3–53; e: sample 18–908; f: sample Y3–27; g: sample Y3–36; h: sample Y3–48; i: sample 18–912. Hu-huminite, Fu-fusinite, Sp-sporinite, Te-telalginite, R-resinite, Se-semifusinite, La-lamalginite, Li-liptodetrinite, P-pyrite.

ranging from 0.90 to 11.91 (Table 3). The C_{24} tetracyclic terpane (Tet) is present in lesser amounts than the C_{23} and C_{26} Tri with the ratios of C_{24} Tet/C_{23} Tri and C_{24} Tet/C_{26} Tri being 0.15–0.40 and 0.21–0.97, respectively (Fig. 4c and d; Table 3). Furthermore, Tri concentration exhibits little correlation with TOC content as compared to other compounds.

A series of hopanes, ranging from C_{27} to C_{35} with the exception of C_{28}, was observed in the studied samples and includes multiple stereoisomers (Fig. 4c and d). The distribution of hopanes is variable. For the samples from the Y 3 well, the identified hopanes include C_{27}-C_{31} 7β(H),21β(H) -hopanes (ββ hopanes) (even to C_{32} ββ in some samples), C_{29}-C_{30} 7β(H),21α (H)-hopanes (βα hopanes), and C_{27}-C_{32} 7α(H),21β(H)-hopanes (αβ hopanes) with C_{29} ββ being the dominant compound. Besides, hopenes including C_{27} 17β(H)-22,29,30-Trisnorhopane (βTm), 29 and 30 neohop-13 (18)-enes, and 30 hop-17 (21)-ene are observed. In contrast, the samples from the H 1 well exhibit a relatively higher abundance of gammacerane (Gamm) and C_{32-35} αβ hopanes, while hopenes and ββ hopanes are missing. Moreover, two series of methylhopanoids (MeH) (*m/z* 205) including *2α*-MeH and *3β*-MeH can be detected in all studied samples with *2α*-C_{30} MeH/C_{30} αβ hopane ranging from 0.11 to 0.53 and *3β*-C_{30} MeH/C_{30} αβ hopane ranging from 0.12 to 2.82 (Table 3). In addition, low concentrations of C_{29} 25-norhopane (C_{29} NH) are detected in all samples with C_{29} NH/C_{30} αβ hopane ratios of 0.03–0.23 and with 46% greater than 0.10 (Table 3).

4.4.3. Steroids and sterenes

Steroids, and lanostanes as well as sterenes were observed in all samples by monitoring the *m/z* 217, *m/z* 259 (Fig. 4e and f), and *m/z* 257 ion chromatograms (Fig. 4g and h). Among the identified compounds, C_{29} steranes (39–80%) are most abundant, followed by C_{27} steranes (6–46%) in most cases (Fig. 4e and f) (Table 3). It is noteworthy that C_{27} and C_{28} steranes display smaller concentrations in the H 1 well as compared to the Y 3 well in most of the cases. C_{29} ααα20S/(20S + 20R) ratios are similar in the samples from the two wells, which range from 0.01 to 0.22 (Table 3). Moreover, C_{29} αββ/(αββ + ααα) ratios for the Y 3 well are generally smaller than 0.3 in most cases (ranging from 0.12 to 0.35 with an average value of 0.19), whereas for the H 1 well, they are greater than 0.3 in most cases (i.e., ranging from 0.21 to 0.38 with an average value of 0.32) (Table 3).

In addition, C_{30} 4-methylsteranes can be detected in these late Neogene sediments. Among 4-methylsteranes, dinosteranes are more abundant than 4- and 24- substituted methylsteranes. Moreover, pregnane and homopregnane can be detected in low abundance (Fig. 4e and f).

4.4.4. Aromatic hydrocarbons

A series of mononuclear aromatic and 2- to 6-ring polynuclear aromatic hydrocarbons (PAHs) were identified in the samples (Fig. 5 and Fig. 6).

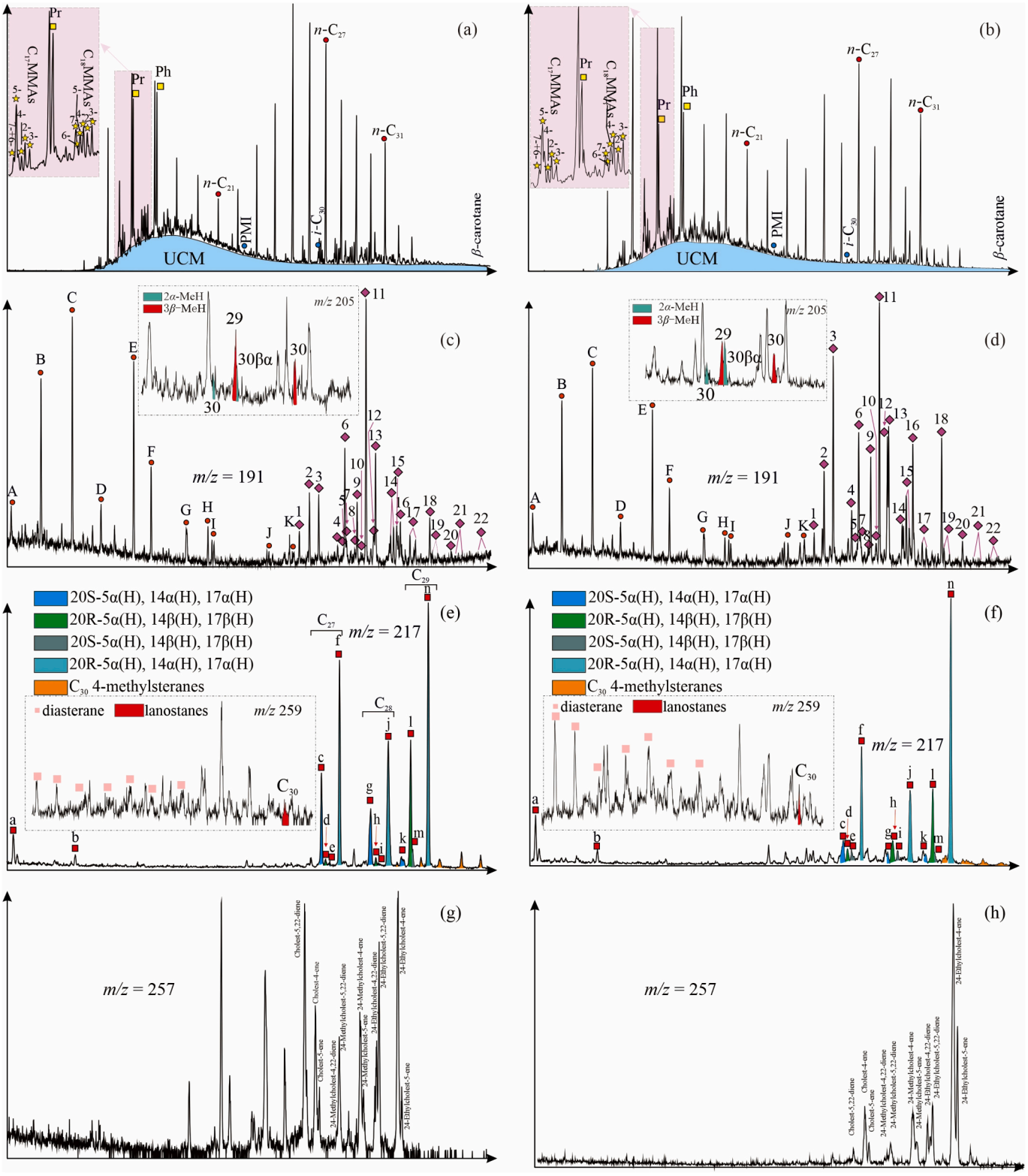

Fig. 4. Distribution of partial mass chromatograms of the aliphatic fraction in representative samples (figures on the left represent sample H 18–906, and those on the right sample Y 3–18). (a–b) Total ion chromatogram (TIC); (c–d) Mass chromatograms showing the distribution of terpanes (*m/z* 191) and methylhopanoids (*m/z* 205); (e–f) Mass chromatograms showing the distribution of steranes (*m/z* 217) and lanostanes (*m/z* 259); (g–h) Mass chromatograms (*m/z* 257) showing the distribution of sterenes. See Appendix (Table A1) for detailed peak identification.

Mononuclear aromatic compounds detected in this study are methyltrimethyltridecylchromans (MTTCs) including 2,8-dimethyl-2-(4,8,12-trimethyltrisecyl) -chromatid (*δ*-MTTC; *m/z* 121), 2,5,7-trimethyl-2- (4,8,12-trimethyltrisecyl) -chromatid (*ζ*-MTTC), 2,7,8-trimethyl-2- (4,8,12-trimethyltrisecyl) -chromatid (*γ*-MTTC), 2,5,8-trimethyl-2- (4,8,12-trimethyltrisecyl) -chromatid (*β*-MTTC) (*m/z* 135), and 2,5,7,8-tetramethyl-2- (4,8,12-rimethyltrisec-yl) -chroma (*α*-MTTC; *m/z* 149). The 2-ring polynuclear compounds mainly include

Table 2
Biomarker parameters of alkane hydrocarbon for the sediments from the Shizigou Formation in the Yiliping Depression, Qaidam Basin, China.

Well	Sample ID	Main peak of normal alkane	Pr/Ph	Pr/*n*-C_{17}	Ph/*n*-C_{18}	CPI_{12-20}	CPI_{24-34}	*n*-C_{17}/(*n*-C_{23} + *n*-C_{25} + *n*-C_{27})	TAR	Paq	*n*-C_{17}/*n*-C_{27}	*β*-carotanes/*n*-C_{25}	Squalene/*n*-C_{22}	PMI/*n*-C_{26}	ACL	HD/D
Y 3	Y3–1	*n*-C_{16}	1.07	0.78	0.69	0.65	4.27	1.34	0.68	0.30	2.94	0.69	0.32	0.75	28.42	6.67
	Y3–5	*n*-C_{16}	1.01	0.83	1.04	0.70	3.39	0.83	0.84	0.46	2.26	0.20	0.16	0.89	27.45	17.79
	Y3–18-917	*n*-C_{27}	0.49	0.86	1.19	1.02	1.44	0.07	6.59	0.51	0.14	0.05	0.12	0.19	27.24	6.09
	Y3–16	*n*-C_{16}	0.94	0.60	0.59	0.63	2.41	0.53	1.38	0.43	1.21	0.12	0.23	0.29	27.40	17.10
	Y3–18	*n*-C_{18}	0.26	1.04	3.05	0.69	3.29	0.31	1.25	0.68	1.04	0.10	0.56	0.44	26.15	6.55
	Y3–19	*n*-C_{29}	0.72	0.98	1.57	0.68	3.93	0.23	3.15	0.40	0.73	0.06	0.28	1.23	27.76	6.43
	Y3–26	*n*-C_{16}	0.63	0.73	1.04	0.67	5.94	0.63	1.85	0.28	1.34	0.15	0.41	2.69	28.53	21.51
	Y3–27	*n*-C_{16}	1.19	0.89	1.30	0.78	5.69	2.60	0.61	0.18	4.27	0.50	0.18	1.37	28.95	7.97
	Y3–36	*n*-C_{16}	0.44	1.62	6.30	0.86	4.13	0.42	1.01	0.48	1.15	2.57	0.70	1.25	27.52	2.18
	Y3–40	*n*-C_{18}	0.63	1.13	0.93	0.83	2.72	1.07	0.62	0.40	2.81	0.35	0.52	1.19	27.63	2.83
	Y3–44	*n*-C_{16}	0.51	1.36	5.25	0.86	4.35	0.17	2.79	0.48	0.43	0.11	0.42	0.53	27.26	2.66
	Y3–45	*n*-C_{29}	0.77	1.08	1.76	0.84	3.94	0.15	3.25	0.36	0.34	0.08	0.34	0.52	27.86	2.72
	Y3–48	*n*-C_{29}	0.43	0.79	6.28	1.60	4.17	0.17	3.51	0.46	0.45	0.17	0.43	0.86	27.44	1.81
	Y3–53	*n*-C_{29}	0.98	0.72	0.88	0.74	2.95	0.28	2.37	0.40	0.71	0.05	0.14	0.14	27.70	5.35
	Y3–55	*n*-C_{27}	0.82	0.83	1.42	0.83	4.21	0.14	2.77	0.59	0.37	0.16	0.18	0.64	26.86	3.97
H 1	18–905	*n*-C_{25}	0.78	0.89	1.03	0.80	1.37	0.30	1.53	0.65	0.87	0.09	0.30	0.33	26.79	14.13
	18–906	*n*-C_{25}	0.99	0.86	0.99	0.83	1.29	0.31	1.83	0.62	0.82	0.07	0.23	0.12	26.84	6.85
	18–907	*n*-C_{18}	0.90	0.85	1.05	0.85	2.90	1.70	0.51	0.42	5.46	0.90	0.51	1.21	28.10	12.80
	18–908	*n*-C_{25}	1.08	0.92	1.12	0.84	1.45	0.37	1.51	0.61	1.02	0.04	0.21	0.12	27.01	21.14
	18–909	*n*-C_{18}	0.82	0.81	1.00	0.84	3.49	1.91	0.46	0.39	6.22	0.75	0.53	1.41	28.30	8.15
	18–910	*n*-C_{16}	1.09	0.74	0.83	0.64	3.27	1.04	0.75	0.44	2.23	0.36	0.30	0.65	27.37	38.36
	18–911	*n*-C_{27}	0.75	0.86	1.26	0.84	1.40	0.55	0.89	0.65	1.67	0.01	0.21	0.19	26.46	14.87
	18–912	*n*-C_{17}	0.90	0.93	1.18	0.86	1.47	0.50	0.96	0.64	1.44	0.05	0.32	0.13	26.83	11.00
	18–913	*n*-C_{25}	0.88	0.83	1.05	0.70	1.85	0.90	0.73	0.58	2.36	0.01	0.31	0.52	26.58	17.14

Note: main peak = the highest peak height; Pr = pristane; Ph = phytane; CPI_{12-20} = carbon preference index for *n*-alkanes = 2 × ∑odd (*n*-C_{13}–*n*-C_{19})/[∑even (*n*-C_{12}–*n*-C_{18}) + ∑even (*n*-C_{14}–*n*-C_{20})]; CPI_{24-34} = carbon preference index for *n*-alkanes = 2 × ∑odd (*n*-C_{25}–*n*-C_{33})/[∑even (*n*-C_{26}–*n*-C_{34}) + ∑even (*n*-C_{24}–*n*-C_{32})]; ACL = [(23 × *n*-C_{23}) + (25 × *n*-C_{25}) + (27 × *n*-C_{27}) + (29 × *n*-C_{29}) + (31 × *n*-C_{31})]/(*n*-C_{23} + *n*-C_{25} + *n*-C_{27} *n*-C_{29} *n*-C_{31}); TAR = (*n*-C_{27} + *n*-C_{29} + *n*-C_{31})/(*n*-C_{15} + *n*-C_{17} + *n*-C_{19}); Paq = (*n*-C_{23} + *n*-C_{25})/(*n*-C_{23} + *n*-C_{25} + *n*-C_{29} + *n*-C_{31}).

naphthalene (N; 128), methylnaphthalenes (MNs; 142), biphenyls (BP; *m/z* 154), ethylnaphthalenes + dimethylnaphthalenes (ENs + DMNs; *m/z* 156), trimethylnaphthalenes (TMNs; *m/z* 170), and tetramethylnaphthalenes (TeMNs; *m/z* 184). The 3-ring polynuclear aromatic compounds are mainly diphenylmethane + methylbiphenyls + dibenzofurane (MBps + DPM + DBF; *m/z* 168), fluorene (Fl; *m/z* 166), cadalene (Cad; *m/z* 183), methylfluorenes (MFs; *m/z* 180), dibenzothiophene (DBT; *m/z* 184), phenanthrene (PHE; *m/z* 178), methyldibenzothiophenes (MDBTs; *m/z* 198); methylphenanthrenes (MPs; *m/z* 192), ethylphenanthrenes + dimethylphenanthrenes (EPs + DMPs; *m/z* 206), retene (Ret; *m/z* 219), trimethylphenanthrenes + ethylphenanthrenes + methylphenanthrenes + C_3-phenanthrene (TMPs + EPs + MPs + C_3-P; *m/z* 220), triaromatic steroids (TAS; *m/z* 231 shown in Fig. 6a and b) as well as methyltriaromatic steroids and C_{29} 4α,23,24-trimethyltriaromatic steroids (MeTAS and dino-TAS; *m/z* 245 shown in Fig. 6c and d). The 4-ring polynuclear aromatic compounds are mainly fluoranthene + pyrene (Fla + Py; *m/z* 202), methyl fluoranthenes + benzo[*a*]fluorene + benzo[*b*]fluorene + methylpyrenes (MFla + BaF + BbF + MPys; *m/z* 216), chrysene (Chr; *m/z* 228), and 9- + 2-methylretenes (Mrets; *m/z* 233). The 5-ring polycyclic aromatic compounds mainly include benzo[*b*]fluoranthene, benzo[*e*]pyrene, benzo[*a*]pyrene, and perylene (Pery; *m/z* 252). Parameters used for characterization of higher plants including higher plant index (HPI = (Retene + Cadalene + ip-iHMN)/1,3,6,7-TeMN) (van Aarssen et al., 1996), and higher plant parameter (HPP = retene/(retene + cadalene) (van Aarssen et al., 2000) are 0.36–22.14 (4.30 on average) and 0.15–1.00 (0.59 on average) (Table 4).

5. Discussion

5.1. Thermal maturity

Generally, a significant amount of OM which is thermally immature or very early thermally mature is necessary for the formation of microbial CH_4 (VR_r <0.6%) (Schoell, 1980). Both the T_{max} and petrographic VR_r values illustrate that the OM in source rocks studied are thermally immature (i.e., T_{max} <435 °C and VR_r <0.5%; Peters et al., 2005) with very few samples being just at the limit to the early thermally mature stage. This is consistent with the presence of typical immature molecular biomarkers, including hopane/hopene series including βTm, C_{29-31} 17β (H),21β (H)-hopanes, neohop-13(18)-enes, C_{30} hop-17 (21)-ene, and 4β-methylsteranes (Mackenzie et al., 1980; Ten Haven et al., 1986; Sinninghe Damsté et al., 2014; Volkman et al., 2015; Synnott et al., 2021), as well as sterenes and steradienes (Amo et al., 2007; Killops and Abbott, 2022; Synnott et al., 2023) (Fig. 4g and h). This thermal maturity, which is close to that of the overlying Pleistocene Qigequan Formation (Qiao et al., 2021a), indicates that the OM in the late Neogene Shizigou Formation possesses the potential for significant microbial gas generation (Schoell, 1980).

5.2. Biological sources of organic matter

5.2.1. Evidence from programmed open-system pyrolysis and maceral composition

Based on microscopic observation, the origin of OM in the samples with high TOC content from the Y 3 well is complex. Sporinite, which may originate from various types of plants including pteridophytes, gymnosperms, angiosperms, and bryophyte spores (Pickel et al., 2017), is common in these samples (Fig. 3f, g, and h), indicating an assemblage of OM derived from higher land plants in fluvio-deltaic ecosystems close to the lake. The OM in these samples also contains inertinite, e.g., semifusinite (Fig. 3b) and fusinite (Fig. 3c and d), indicating charcoal derived from higher plants making contributions to the OM (ICCP, 2001). A terrestrial contribution is further supported by the presence of resinite (Fig. 3f, g, and h) and huminite (Fig. 3a, b, and c) (ICCP, 1998; Pickel et al., 2017). Among the huminite, ulminite B, which is derived

Table 3
Biomarker parameters of terpanes and steranes for the sediments from the Shizigou Formation in the Yiliping Depression, Qaidam Basin, China.

Well	Sample ID	Tri and Tet							Hopanes, methylhopanes (MeH) and gammacerane (Gamm)						Sternane				Normalized distribution of sternanes (%)			Sternanes/ hopanoids
		$C_{19}/(C_{19}+C_{23})$ Tri	C_{22}/C_{21} Tri	C_{24}/C_{23} Tri	C_{26}/C_{25} Tri	C_{24} Tet/C_{23} Tri	C_{24} Tet/C_{26} Tri	ETR	Gamm/C_{30} (αβ + ββ) hopane	C_{31} 22 R/C_{30} αβ hopane	C_{31} S/(S + R) hopane	C_{29} NH/C_{30} αβ hopane	2α-C_{30} MeH/C_{30} αβ hopane	3β-C_{30} MeH/C_{30} αβ hopane	C_{21-22}/C_{27-29} steranes	C_{27} diasteranes/ regular steranes	Sterane C_{29} ββ/(ββ + αα)	Sterane C_{29} ααS/(S + R)	C_{27}	C_{28}	C_{29}	
Y 3	Y3–1	0.25	0.20	0.54	1.25	0.28	0.52	1.62	0.17	0.15	0.56	0.20	0.20	0.21	0.10	0.56	0.35	0.22	27	24	49	0.30
	Y3–5	0.30	0.18	0.53	0.90	0.20	0.43	5.28	0.09	0.22	0.27	0.14	0.14	0.33	0.02	0.15	0.17	0.02	25	26	49	1.26
	Y3–18-917	0.16	0.19	0.54	0.91	0.28	0.84	1.41	0.05	0.16	0.26	0.05	0.21	0.44	0.01	0.04	0.16	0.02	20	19	61	2.14
	Y3–16	0.28	0.20	0.49	0.83	0.17	0.56	4.01	0.13	0.26	0.34	0.21	0.18	0.38	0.07	0.31	0.24	0.05	22	21	57	0.75
	Y3–18	0.11	0.22	0.59	0.91	0.23	0.49	6.09	0.10	0.60	0.19	0.15	0.13	0.12	0.01	0.07	0.12	0.01	16	19	65	0.93
	Y3–19	0.29	0.19	0.54	0.70	0.26	0.65	9.57	0.11	0.37	0.15	0.23	0.45	0.63	0.01	0.13	0.12	0.02	12	20	68	0.51
	Y3–26	0.27	0.19	0.56	0.77	0.23	0.47	4.17	0.05	0.06	0.41	0.07	0.11	0.22	0.01	0.11	0.15	0.08	10	15	75	2.05
	Y3–27	0.40	0.16	0.49	0.78	0.26	0.43	6.34	0.08	0.05	0.35	0.09	0.13	0.14	0.01	0.09	0.16	0.10	10	16	74	1.33
	Y3–36	0.46	0.07	1.25	0.67	0.21	0.21	1.85	0.16	0.05	0.29	0.03	0.12	0.37	0.00	0.01	0.17	0.01	12	21	67	3.15
	Y3–40	0.15	0.24	0.50	0.98	0.19	0.52	2.18	0.11	0.27	0.33	0.17	0.24	0.33	0.05	0.16	0.30	0.03	25	13	62	2.03
	Y3–44	0.30	0.11	0.79	0.75	0.24	0.33	9.84	0.10	0.35	0.10	0.09	0.23	1.52	0.00	0.02	0.19	0.01	14	18	68	1.59
	Y3–45	0.27	0.19	0.55	0.81	0.24	0.51	8.05	0.15	0.28	0.22	0.13	0.34	2.75	0.01	0.06	0.19	0.01	16	17	67	1.05
	Y3–48	0.31	0.18	0.70	0.79	0.40	0.54	11.91	0.14	0.24	0.22	0.08	0.53	2.63	0.00	0.02	0.17	0.01	11	18	71	2.05
	Y3–53	0.37	0.19	0.56	0.93	0.40	0.92	7.20	0.10	0.35	0.21	0.18	0.20	2.82	0.04	0.30	0.21	0.02	10	15	75	0.42
	Y3–55	0.31	0.17	0.62	0.96	0.29	0.47	4.60	0.16	0.12	0.25	0.04	0.25	1.03	0.00	0.05	0.20	0.00	6	14	80	4.36
H 1	18–905	0.18	0.24	0.45	0.79	0.17	0.90	2.15	0.16	0.25	0.40	0.15	0.22	0.40	0.20	0.23	0.36	0.11	29	20	51	1.04
	18–906	0.18	0.22	0.45	0.78	0.18	0.82	0.90	0.13	0.13	0.40	0.08	0.16	0.32	0.05	0.08	0.34	0.04	30	27	43	2.41
	18–907	0.17	0.24	0.50	0.80	0.19	0.72	1.83	0.14	0.19	0.45	0.10	0.26	0.38	0.09	0.18	0.38	0.06	28	19	53	1.00
	18–908	0.22	0.20	0.47	0.74	0.18	0.88	1.52	0.08	0.41	0.24	0.09	0.21	0.33	0.11	0.11	0.32	0.05	44	12	44	0.82
	18–909	0.12	0.25	0.50	0.69	0.15	0.68	2.40	0.12	0.23	0.36	0.12	0.27	0.34	0.13	0.19	0.35	0.04	29	18	53	1.27
	18–910	0.30	0.18	0.49	1.00	0.27	0.70	4.12	0.19	0.17	0.30	0.17	0.13	0.31	0.07	0.41	0.21	0.05	19	25	56	0.95
	18–911	0.23	0.22	0.46	0.74	0.15	0.82	1.36	0.12	0.29	0.37	0.02	0.15	0.32	0.06	0.04	0.29	0.04	46	15	39	2.12
	18–912	0.22	0.22	0.45	0.69	0.15	0.97	1.56	0.09	0.40	0.24	0.07	0.23	0.40	0.08	0.07	0.32	0.03	40	12	48	1.30
	18–913	0.29	0.20	0.43	0.72	0.20	0.81	1.49	0.11	0.40	0.28	0.03	0.27	0.27	0.05	0.08	0.31	0.04	37	16	47	1.07

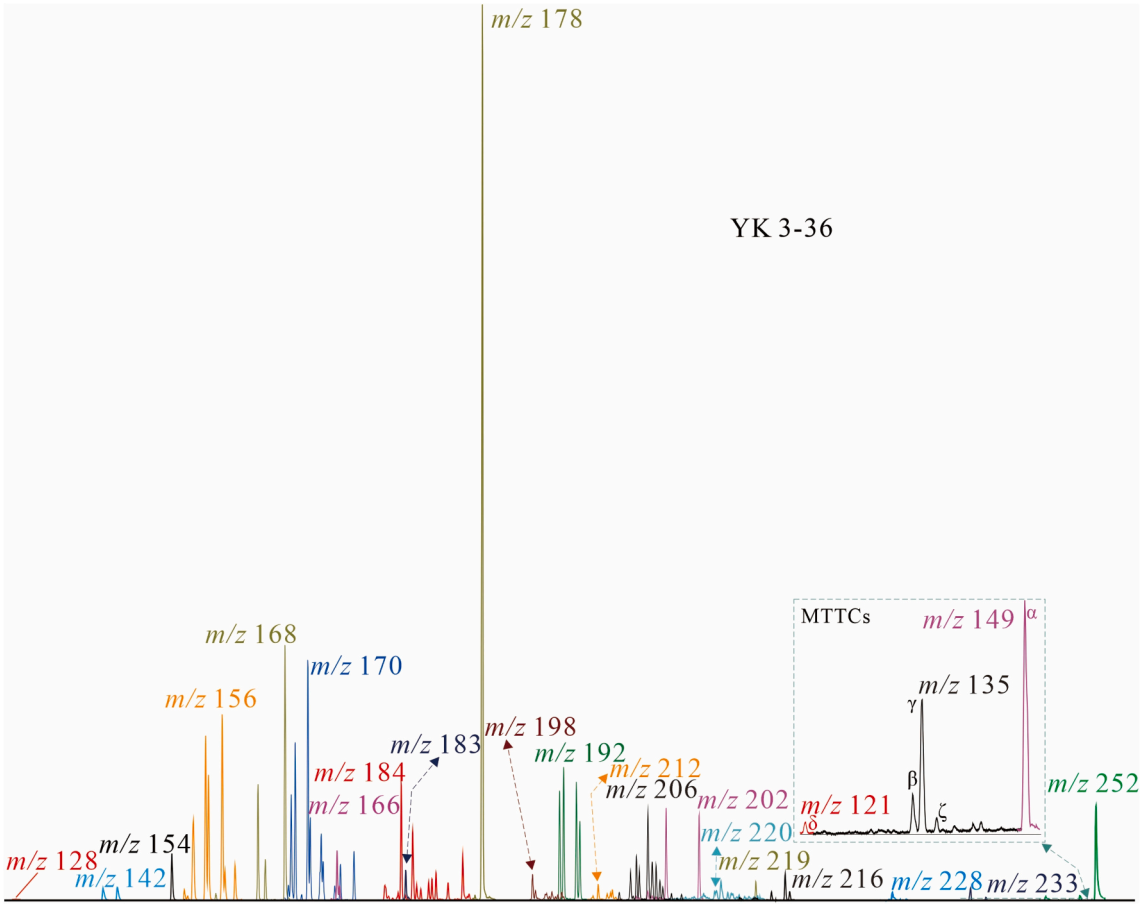

Fig. 5. Partial mass chromatograms for the aromatic fraction of sample YK 3–36. See the text for the explanation of the peaks.

from various angiosperms, is more abundant than ulminite A derived from gymnosperms (Sýkorová et al., 2005). The observation of lamalginite and liptodetrinite (Fig. 3g) indicates that algae/other phytoplankton also make a minor contribution to the OM (Pickel et al., 2017). In contrast, the samples with low TOC content in the H 1 well exhibit fragmented macerals, i.e., rather small huminite particles (Fig. 3d and e) as well as lamalginite (Fig. 3i).

According to the programmed open-system pyrolysis data, the kerogen of the analyzed samples from the Y 3 well is composed of mixed types II–III (Fig. 7a and b) (Pepper and Corvi, 1995). It is important to note that the kerogen type of the samples from the H 1 well is typical type III kerogen, which exhibits lower HI values compared to both the kerogen type of the Pleistocene H 1 well samples and the late Neogene Y 3 well samples. The lower HI values of the late Neogene Shizigou samples compared to the Pleistocene samples can be attributed to the low TOC content, which leads to the mineral matrix effect (MME) during the programmed open-system pyrolysis, and lowers the true S_2 and HI values, particularly in samples with TOC contents of less than 2% (Espitalié et al., 1985; Grohmann et al., 2019; Beti et al., 2021). However, it is important to note that even after correcting the HI values of the studied sample using the method proposed by Behar et al. (2021) based on the ratio of HI measured on whole rock to that measured on isolated OM, the corrected HI values still indicate a typically detrital input without a major contribution of hydrogen-rich algal OM. Thus, it is plausible that the low HI values are a result of significant OM degradation, as discussed in section 5.4. It should be noted that TOC, S_1, S_2, and HI values in the samples from the late Neogene Shizigou Formation are generally lower than those from the Pleistocene sediments (Qiao et al., 2021a), indicating that the late Neogene Shizigou Formation has less potential to generate large amounts of microbial gas compared to the Pleistocene sediments.

In summary, maceral composition is closely linked to the TOC content. The samples with high TOC content, primarily from the Y 3 well, exhibit a greater contribution of higher plant to the OM and are representative of type III kerogen. In contrast, the low TOC samples contain few macerals from higher plants but display abnormally low HI values, which cannot be attributed to the original composition of the OM.

5.2.2. *Evidence from aliphatic hydrocarbons*

In general, thermal maturity has a significant impact on the distribution of *n*-alkanes. The low thermal maturity of the studied sequence ensures the reliability of the biomarkers in the interpretation of the organism's composition. The short-chain *n*-alkanes ($n \leq 20$) are predominantly sourced from cyanobacteria or algae/phytoplankton, and maximum peaks occurring at odd carbon and even carbon numbers indicate algae and bacterial input, respectively (Cranwell, 1977; Meyers and Ishiwatari, 1995). The *n*-C_{17} peak is mainly prominent in the samples from the H 1 well, while the samples from the Y 3 well show a prominent *n*-C_{16} peak. Furthermore, the CPI_{12-20} values <1 for most studied samples are possibly related to massive microbial input (Clark and Blumer, 1967; Ahad et al., 2011). Microbial and algal contributions can be also deduced from the occurrence of branched alkanes (*br*-alkanes) and bicyclic alkanes as well as hopanoids (Alexander et al., 1983; Alexander et al., 1984; Shiea et al., 1990) (Fig. 4a-b).

Among the intermediate-molecular-weight *n*-alkanes ($21 \leq n \leq 25$), *n*-C_{25} exhibit the highest peaks in the samples from the H 1 well. These *n*-alkanes not only originate from lower organisms, such as phycophyta (Mead et al., 2005; Riboulleau et al., 2007) and photosynthetic bacteria (dos Santos Neto et al., 1998), but also hydrophilous macrophytes, e.g., aquatic pollen taxa, Sphagnum mosses, Ruppia, and freshwater

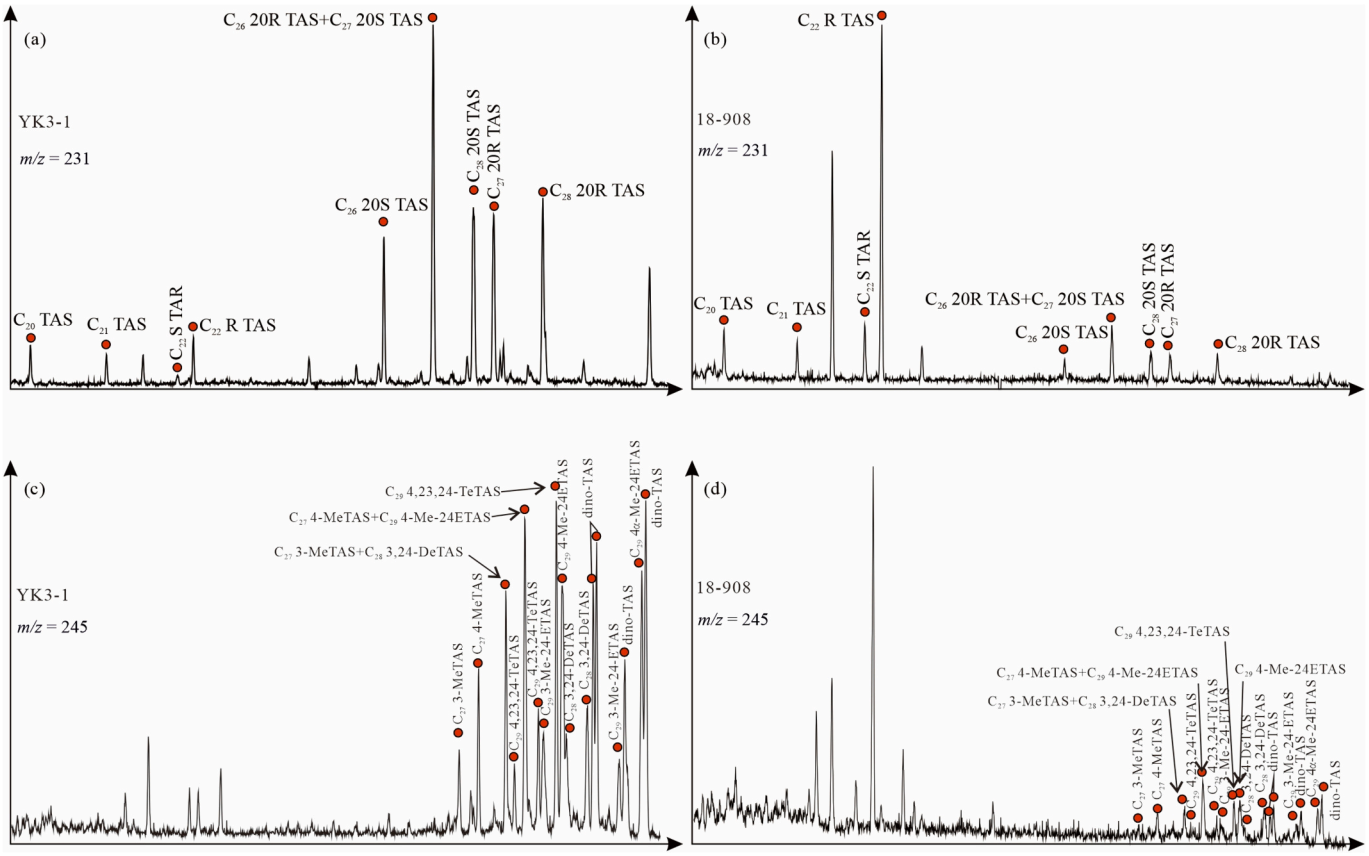

Fig. 6. Representative mass chromatograms (*m/z* 231) of the TAS and (*m/z* 245) of the MeTAS and dino-TAS. Notes: TAS = triaromatic steroids; MeTAS = methyltriaromatic steroids; DeTAS = dimethyltriaromatic steroids; TeTAS = trimethyltriaromatic steroids; Me-24ETAS = methyl-24-ethyltriaromatic steroids; dino-TAS = C_{29} 4α,23,24-trimethyltriaromatic steroids.

Nymphaea (Mead et al., 2005; Coetzee, 1967; Bingham et al., 2010; He et al., 2020). Long-chain *n*-alkanes ($n \geq 26$), mainly derived from waxes of woody higher land plants (Pearson and Eglinton, 2000), show the peak at *n*-C_{27} or *n*-C_{29} in the samples from the Y 3 well.

The presence of short-chain monomethylalkanes (MMAs) in most samples from the two wells is indicative of the existence of cyanobacteria within microbial mats (Sinninghe Damsté et al., 1995; Kenig, 2000; Bauersachs et al., 2009; Pawlowska et al., 2013), which is consistent with the identified 2-MeHs, i.e., the signature of cyanobacterial biomass (Farrimond et al., 2004). Besides, long-chain MMAs, which may be mainly associated with microorganisms or heterotrophic bacteria rather than cyanobacteria (Lu and Sun, 2003), can be observed in the samples without clear odd and even predominance (i.e., samples from the H 1 well) in the late Neogene sediments. It is worth noting that the presence of long-chain MMAs has also been observed in the Pleistocene organic facies B samples from the Qaidam Basin, which were deposited in an oxic, brackish-lacustrine water body with OM origins from saltwater algae and some additional bacteria (Qiao et al., 2021a).

In addition, algae and bacteria can be identified by some specific biomarkers present in most samples, e.g., PMI and squalene which are the primary components of the membrane lipids of methanogens and halophilic archaea (Peters et al., 2005; Volkman et al., 2015), and C_{30} 4-methylsteranes, which are closely associated with dinoflagellates inhabiting fresh and brackish water columns (Fu et al., 1993; Horsfield et al., 1994; Bechtel et al., 2012). Moreover, the abundances of C_{30} 4-methylsteranes are high in the samples, indicating that dinoflagellates made a greater contribution to the OM. This finding is consistent with the higher abundances of MeTAS and dino-TAS in the samples, because they are indicative of modern marine dinoflagellates (Fig. 6; Peters et al., 2005). The occurrence of C_{29} neohop-13 (18)-ene and C_{29} hop-17 (21)-ene indicates methanotrophs and C_{30} hop-17 (21) -ene indicates of methanotrophs mixed with other bacteria (Volkman et al., 2015). Methanotrophs, a branch of methyl-oxidizing bacteria, can utilize methane as the only energy and carbon source. The detection of 3-MeH, which are synthesized from methanotrophs during diagenesis, indicates a significant input of methanogens (Farrimond et al., 2004).

Specifically, $CPI_{24–34}$ values of <5 and >5 are indicative of aquatic higher plants and terrestrial higher plants, respectively (Bechtel et al., 2012; Bechtel et al., 2013). Here, the low $CPI_{24–34}$ values might indicate the possibility of microbial decomposition of OM and input of saltwater algae (Bechtel et al., 2001; Qiao et al., 2021a). The $CPI_{24–34}$ values of the samples from the Y 3 well, even for the samples with low TOC content (e.g., Y 3–1, Y3–5 and Y 3–55), indicate significant contributions from aquatic higher plants to the OM composition, while the OM of the H 1 samples contains abundant saltwater algae.

Paq was proposed as a tool to investigate OM origins based on of middle- and high-molecular-weight *n*-alkanes. Terrestrial higher plant lipids are characterized by Paq values less than 0.1, emergent communities by 0.1–0.4, and submerged/floating vegetation by 0.4–1.0 (Ficken et al., 2000). The Paq values infer that the OM in most samples was largely derived from submerged/floating macrophytes rather than terrestrial higher plants, while emergent macrophytes contributed to the OM only in some samples from the Y 3 well. TAR and *n*-C_{17}/*n*-C_{27} show substantial variations in the samples from both the H 1 well and Y 3 well, implying the respective contributions of different types of OM. In addition, the Paq is negatively correlated to the ACL (R^2 = 0.93) but positively correlated to the middle-chain *n*-alkanes concentration (R^2 = 0.75) (Fig. 8), indicating that submerged rather than terrestrial higher plants were predominant contributors to the OM. In comparison to the Pleistocene samples, the late Neogene Shizigou samples have higher Paq

Table 4
Aromatic parameters for the sediments from the Shizigou Formation in the Yiliping Depression, Qaidam Basin, China.

well	Sample ID	HPI	HPP	log (1,2,7-TMN/1,3,7-TMN)	log (1,2,5-TMN/1,3,6-TMN)	log (1-MP/9-MP)	log (Retene/9-MP)	log [1,7-DMP/(1,3- + 3,9- + 2,10- + 3,10-DMP)]	MTTC ratio	DBT/PHE	1,6-DMN/1,5-DMN	1,3,6-TMN/1,2,4-DMN	1,3,6,7-TeMN/1,3,5,7-TeMN	Normalized distributionof DBT, DBF and FL (%)			C_{26}/C_{28} 20S triaromatic steroid	$(C_{20} + C_{21})/(C_{20} + C_{21} + C_{26} + C_{27} + C_{28})$ triaromatic steroid	$C_{20}/(C_{20} + C_{28}(20R))$ triaromatic steroid
														Fl	DBT	DBF			
Y 3	Y3–1	1.29	0.62	−0.60	−0.18	−0.10	−1.06	−0.41	0.41	0.05	5.99	1.70	1.65	7	68	25	0.53	0.05	0.13
	Y3–5	1.60	0.48	−0.29	−0.11	−0.10	−1.11	−0.37	0.45	0.02	4.19	3.71	1.55	7	85	8	0.71	0.04	0.11
	Y3–18-917	n.d.	1.00	−0.16	0.22	−0.04	−0.60	−0.30	n.d.	0.15	4.69	1.43	0.49	12	58	30	0.47	0.40	0.51
	Y3–16	5.81	0.90	−0.35	0.09	−0.09	−0.84	−0.42	0.49	0.03	2.27	3.22	1.79	3	96	1	0.67	0.07	0.19
	Y3–18	n.d.	1.00	−0.43	−0.02	−0.09	−0.22	−0.35	0.79	0.10	6.06	1.78	3.06	9	61	30	0.56	0.07	0.18
	Y3–19	0.85	0.31	−0.79	−0.52	−0.17	−0.78	−0.48	0.58	0.06	7.39	3.83	2.11	13	32	56	0.55	0.09	0.19
	Y3–26	n.d.	1.00	−0.02	0.09	−0.05	−0.40	−0.30	0.26	0.02	3.50	1.85	1.92	6	66	28	0.59	0.11	0.22
	Y3–27	0.86	0.27	−0.53	−0.45	−0.13	−0.80	−0.42	0.24	0.06	9.03	5.44	2.73	19	24	57	0.76	0.07	0.22
	Y3–36	0.36	0.24	−0.73	−0.64	−0.16	−1.00	−0.47	0.56	0.06	9.99	8.69	4.54	13	14	73	0.41	0.07	0.22
	Y3–40	22.14	0.92	−0.40	−0.28	−0.11	−0.52	−0.44	0.30	0.03	7.30	3.06	4.01	8	80	12	0.19	0.06	0.11
	Y3–44	2.27	0.16	−0.55	−0.45	−0.15	−0.87	−0.39	0.59	0.08	9.83	5.93	3.89	17	20	63	0.30	0.06	0.10
	Y3–45	3.19	0.20	−0.50	−0.44	−0.10	−0.91	−0.36	0.45	0.06	8.68	3.58	3.21	16	18	66	0.45	0.06	0.10
	Y3–48	0.90	0.15	−0.65	−0.53	−0.20	−0.90	−0.39	0.59	0.13	11.46	8.22	4.00	22	32	46	0.31	0.08	0.19
	Y3–53	2.09	0.35	−0.64	−0.30	−0.08	−1.02	−0.39	0.45	0.05	8.97	2.65	2.11	9	63	28	0.49	0.05	0.11
	Y3–55	3.28	0.31	−0.50	−0.14	−0.05	−0.88	−0.33	0.54	0.05	6.79	2.68	1.75	13	74	13	0.47	0.06	0.14
H 1	18–905	2.95	0.56	0.14	0.05	−0.09	−0.83	−0.42	0.33	0.04	3.47	1.85	1.78	7	91	2	0.47	0.31	0.50
	18–906	7.50	0.79	0.40	0.01	0.00	−0.67	−0.29	0.32	0.04	3.38	4.01	8.01	1	93	6	0.39	0.52	0.63
	18–907	7.06	0.68	−0.17	0.23	−0.13	−0.58	−0.33	0.24	0.03	2.81	3.88	2.29	2	95	3	0.31	0.02	0.05
	18–908	7.01	0.66	0.23	0.24	−0.08	−0.77	−0.34	0.41	0.03	2.65	2.02	3.69	4	95	1	0.49	0.44	0.58
	18–909	5.01	0.62	0.04	0.01	−0.11	−0.73	−0.39	0.27	0.04	3.98	1.75	4.57	7	86	7	0.54	0.74	0.68
	18–910	5.92	0.91	−0.07	0.06	−0.08	−1.04	−0.40	0.45	0.03	n.d.	3.43	2.81	2	97	1	0.73	0.05	0.15
	18–911	2.86	0.96	0.37	0.07	−0.09	−0.73	−0.30	0.42	0.05	1.18	2.90	3.75	4	95	1	0.18	0.02	0.03
	18–912	4.57	0.40	−0.07	−0.08	−0.11	−0.69	−0.37	0.35	0.05	5.51	1.67	1.74	9	46	46	0.26	0.03	0.05
	18–913	1.29	0.62	0.53	0.44	−0.01	−0.61	−0.25	0.34	0.03	0.84	1.30	8.06	1	97	2	0.20	0.02	0.04

Note: MTTC ratio = α-MTTC/(α- + δ- + β- + γ- + ζ-MTTC); HPI = (retene + cadalene + ip-iHMN)/1,3,6,7-TeMN; HPP = retene/(retene + cadalene).

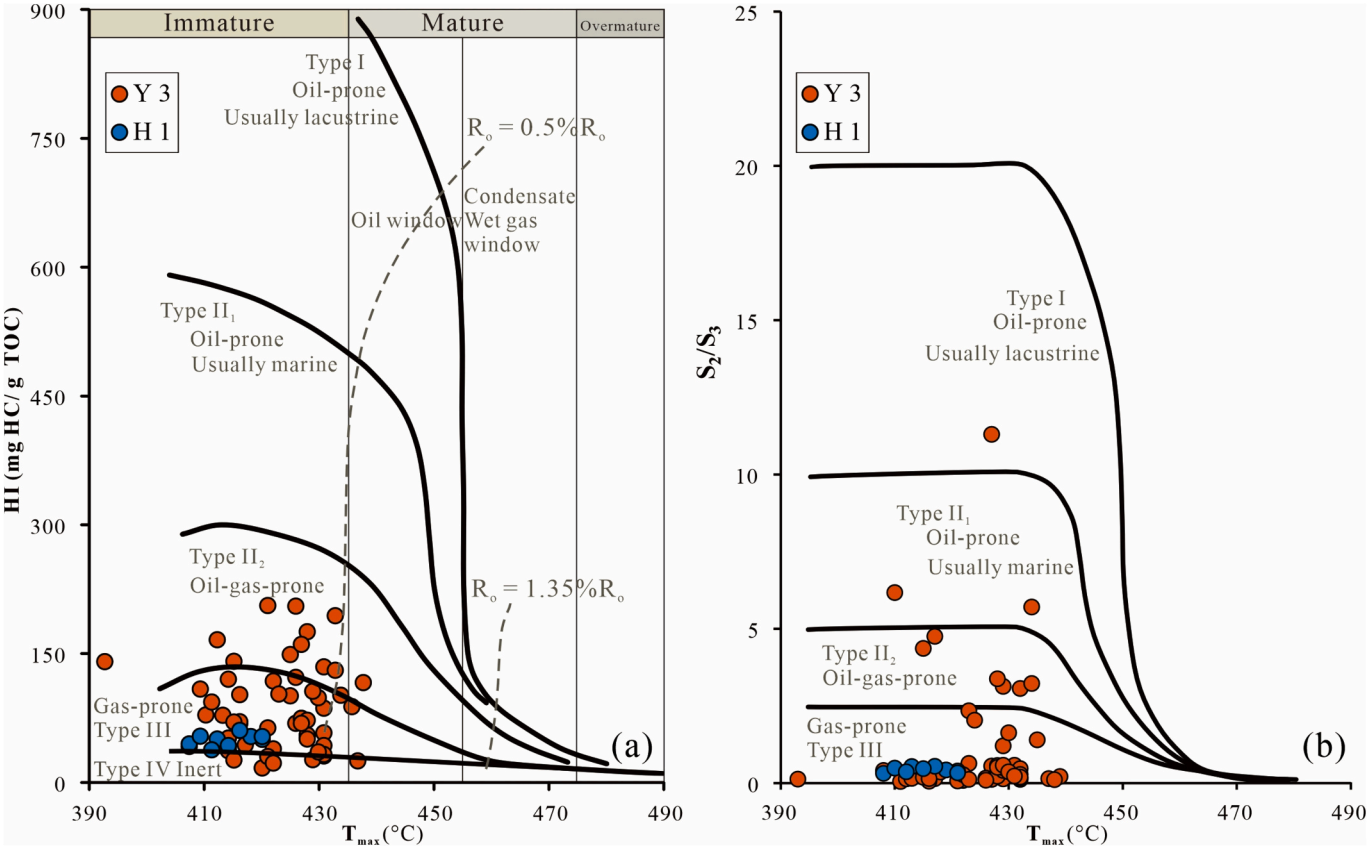

Fig. 7. Cross plots of T_{max} vs. (a) hydrogen index and vs. (b) S_2/S_3 indicating the kerogen type of the sediments from the Shizigou Formation in the Yiliping Depression, Qaidam Basin, China.

values (but below 0.4) and higher TAR values, indicating emergent macrophytes were more prevailing but lower aquatic organisms were less prosperous during the late Neogene period. Thus higher plants that contribute to the OM are mainly aquatic higher plants rather than terrestrial higher plants, as also indicated by other low values of indicators of terrestrial higher plants, i.e., C_{24} Tet/C_{23} Tri and $C_{19}/(C_{19}+C_{23})$ Tri ratios (Table 3) (Philp and Gilbert, 1986; Peters et al., 2005; Volk et al., 2005; Volkman et al., 2015). These two parameters are, however, higher than those in the Pleistocene samples, indicating that relatively more terrestrial higher plants developed during the late Neogene period. Moreover, the concentration of oleanane, being low, further emphasizes the minor contribution of angiosperms (Moldowan et al., 1994) (Fig. 4c and d).

Hopanoids are generally regarded as derived from microbial cell membranes and hopanoids $>C_{30}$ are signatures of cyanobacteria, heterotrophic, and methanotrophic bacteria (Peters et al., 2005; Volkman et al., 2015). The investigated samples contain abundant hopanoids (Fig. 4), indicating microbial lipids contributed to the OM. Furthermore, the occurrence of hop-17 (21)-enes, which also are indicative of eukaryotic phyta or cryptogams (e.g., ferns, mosses, lichens, fungi) (Bottari et al., 1972; Wakeham, 1990; Bechtel et al., 2001; Bechtel et al., 2007), is also observed in the studied samples.

Generally, C_{27}, C_{28}, and C_{29} steranes are inductive of zooplankton, phytoplankton, and terrestrial plants, respectively (Huang and Meinschein, 1979). It is noteworthy that the studied samples show high concentrations of C_{29} steranes in comparison to C_{27} and C_{28} steranes, especially in the Y 3 well samples are reconcilable with the above interpretation because C_{29} steranes are not only derived only from terrestrial higher plants but also from some aquatic plants and microalgae (Huang and Meinschein, 1979; Moldowan et al., 1986; Volkman, 2003; Volkman et al., 2015).

The relative contribution of prokaryotes in comparison to eukaryotes (i.e., higher plants and algae) can be determined by the ratio of hopanoids to steranes. The hopanoids/steranes ratio for the studied samples (listed in Table 3) is slightly lower than that in the Pleistocene Qigequan Formation in the Qaidam Basin (Qiao et al., 2021a), indicating bacteria made a minor contribution to the OM and the bacterial contribution is smaller than in the samples from the Pleistocene sediments.

In summary, the characteristics of aliphatic hydrocarbons indicate that various bacteria, such as halophilic archaea, heterotrophic bacteria, methanotrophic bacteria, methanogens, cyanobacteria, and submerged/floating vegetation play a significant role in contributing to the OM, while terrestrial higher plants contribute only a small amount to the OM in all samples from the H 1 well and Y 3 well. Notably, emergent communities and microalgae contribute more to the OM in the samples from the Y 3 well, while phytoplankton, e.g., saltwater algae, contribute more OM in the samples from the H 1 well.

5.2.3. *Evidence from aromatic hydrocarbons*

Generally, 1,3,6,7-TeMN, an indicator of microbe-derived compound (Jiang et al., 1998), can be detected with high abundances in the studied samples. Cadalene, primarily produced by most vascular plants (Otto and Wilde, 2001; Tu et al., 2003) and possibly also by some procaryotic organisms such as bryophytes, fungi, and algae (van Aarssen et al., 2000), is detected in almost all the samples, indicating a contribution from vascular plants to the OM. Retene and simonellite derived from gymnosperms (Simoneit et al., 1986; Hautevelle et al., 2006) and possibly from algae (Wen et al., 2000; Armstroff et al., 2006) show very low abundances in the samples, indicating a negligible contribution from gymnosperms. Furthermore, the low concentrations below the detection line of ip-iHMN possibly derived from terrigenous higher plants (Ellis et al., 1996), further indicates the small contribution from

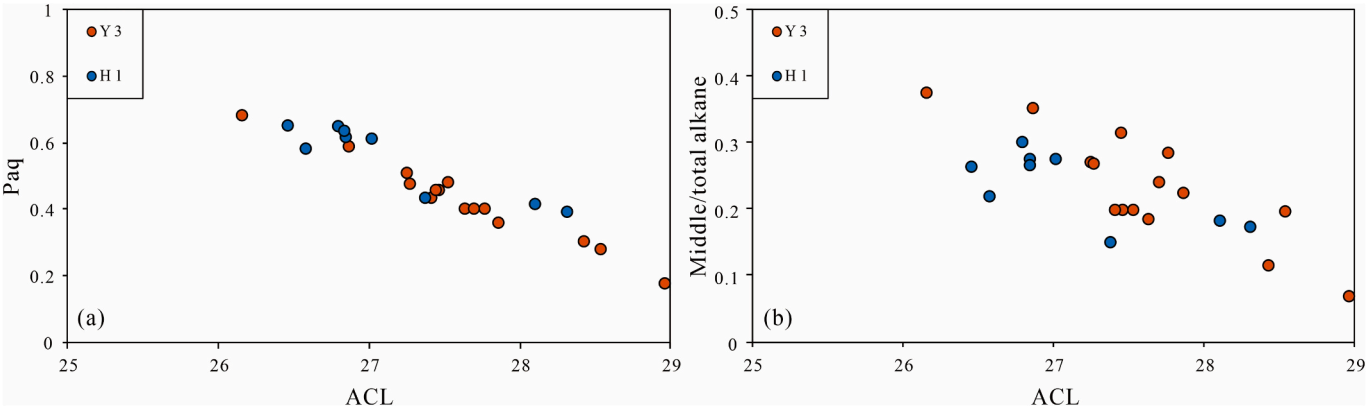

Fig. 8. Cross plots of Paq vs. (a) ACL and vs. (b) middle-chain *n*-alkanes concentration.

terrigenous higher plants to the OM. The low HPI and HPP values further support the above conclusion.

Although the exclusive angiosperm origin of 1,2,7-TMN and terrestrial higher plants (conifer and angiosperms) origin of 1,2,5-TMN were questioned (Strachan et al., 1988; Armstroff et al., 2006; Ellis et al., 1996; Grice, 2001), they are still used as indicators of angiosperm and terrestrial higher plants inputs, respectively. TMNs' abundances are low in all aromatic hydrocarbon fractions, indicating that terrestrial higher plants made little attribution to the OM (Fig. 5). Moreover, the linear relationship observed between log (1,2,7-TMN/1,3,7-TMN) and log (1,2,5-TMN/1,3,6-TMN) (Fig. 9a) might indicate that angiosperms are the primary source of the (small amount of) terrestrial higher plants in the samples, which is consistent with the observation of ulminite B (Sýkorová et al., 2005).

Budzinski et al. (1995) proposed that 9-MP and 1-MP are associated with type Type II to I kerogens and type III kerogen, respectively. Moreover, 1,7-DMP and retene are linked to conifers (van Aarssen et al., 2000; Grice et al., 2005). The cross plots of log (1-MP/9-MP) vs. log (1,2,5-TMN/1,3,6-TMN) (Fig. 9b) and log (Retene/9-MP) vs. log [1,7-DMP/(1,3- + 3,9- + 2,10- + 3,10-DMP)] (Fig. 9c) indicate a low terrestrial OM contribution, as most studied samples are located in the left bottom quadrants. This result is further supported by the low concentrations of other compounds indicative of terrigenous higher plant input including naphthalene, TMPs, chrysene, perylene, cadalane, 9- + 2-Mrets, pyrene, fluoranthene, benzo[*a*]pyrene, benzo[*e*]pyrene, benzo[*b*]fluoranthene, etc. (Chaffee and Johns, 1983; Chaffee and Fookes, 1988; Otto and Wilde, 2001; Haberer et al., 2006; Romero-Sarmiento et al., 2011; Huang et al., 2015).

In summary, aromatics evidence indicates that terrestrial higher plants, primarily angiosperms, contribute little to the OM in all samples.

5.3. Depositional setting

The OM was deposited in a terrestrial, silicate-dominated environment, which is supported by a high abundance of C_{30} αβ hopane as compared to C_{29} αβ hopane (Peters et al., 2005). This is consistent with the low C_{22}/C_{21} and high C_{24}/C_{23} Tri ratios (Fig. 10a; Table 3), which indicate non-carbonate compositions of the analyzed samples. However, the C_{26}/C_{25} Tri vs. C_{31} 22R/C_{30} αβ hopane ratios (Fig. 10b; Table 3) of the studied samples are distributed in the areas of marl, carbonate and marine shale (Peters et al., 2005). This contradiction actually suggests that the mudstone, composed of carbonate and marlstone matrix, formed in a closed basin with no significant surface outlets, under very arid depositional conditions (Goodarzi, 2020b).

The clay-bearing sediments are supported by the cross plot of $C_{27–29}$ sterane concentrations in comparison to $C_{21–22}$ steranes vs. C_{27} regular steranes compared to C_{27} diasteranes (Table 3; Fig. 11) (Qiao et al., 2021b; Zheng et al., 2022). Although αβ homohopane is detected only in some samples owing to the low maturity, the gradual decreasing trend from C_{31} to C_{35} αβ hopanes illustrates clastic facies (Fig. 3c and d) (Qiao et al., 2021b). Additionally, the presence of 4-methylsteranes indicates lacustrine sedimentary environments (Riboulleau et al., 2007). The lower abundance of MDBTs compared to DBF (Hughes, 1984) and MPs (Radke et al., 2000) also supports the non-marine water conditions for the examined samples, which is consistent with the absence of anthracene and benzo[*a*]anthracene (Huang et al., 2015).

5.3.1. Paleoredox conditions

The preservation of OM in depositional environments is controlled not only by paleosalinity, but also by paleoredox conditions. The latter can be assessed using the triangular diagram of TOC-TS-iron (Fig. 12a), which indicates that the majority of samples were formed under an oxygen-rich environment with few high TOC samples, from the Y 3 well deposited under dysoxic bottom water conditions. The paleoredox conditions during the Pleistocene and late Neogene sediments were basically similar.

Paleoredox conditions can be also interpreted by Pr/Ph ratios (Didyk et al., 1978; Liu et al., 2022; Wu et al., 2022; Zheng et al., 2022), with values >3 interpreted as oxic environments above the sediment/water interface, often associated with substantial contributions from higher plants. Values <0.8 indicate anoxic bottom waters usually associated with abundant algae or bacteria. Very low values are typical of salty or carbonate sedimentary environments (Didyk et al., 1978). According to this parameter, the most reducing conditions prevailed during deposition of some samples with high TOC content from the Y 3 well, while the rest and major part was formed under dyoxic or suboxic environments (Fig. 13). However, there are other factors that affect the accuracy of the interpretation based on Pr/Ph, such as different precursor material rather than the phytol side-chain in chlorophyll (e.g., halophilic bacteria; see Ten Haven et al., 1987) and also too low thermal maturity which leads to a lower Pr/Ph (Peters et al., 2005) due to the contribution of halophilic bacteria to phytane.

The Pr/*n*-C_{17} vs. Ph/*n*-C_{18} diagram (Fig. 12b) suggests that most samples were deposited under reducing conditions. For thermally immature sediments, Pr/*n*-C_{17} ratio of <0.5 and >1 typically suggests deposition in open-water and inland swampy environments, respectively (Samad et al., 2020). The Pr/*n*-C_{17} for the studied samples illustrates that most investigated samples were deposited under a mixed environment, while some samples with high TOC content, i.e., some from the Y 3 well located in the margin of the sag, were deposited in or close to an inland swampy environment. This conclusion can be supported by organic petrology as ulminite observed in the samples from the Y 3 well (Fig. 3a, b, and g) is formed primarily in peat and in limnic sediments (Sýkorová et al., 2005). Furthermore, the hypersaline environments characterized by shallow water columns possess the ability to foster the growth of microbial mats which have the potential to isolate

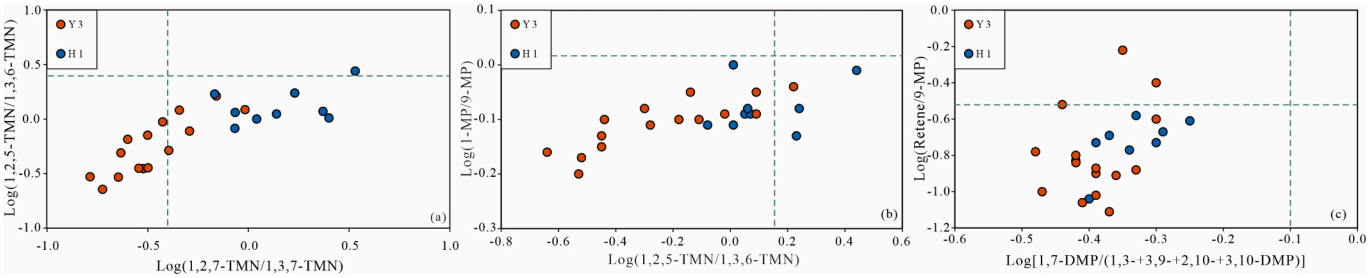

Fig. 9. Cross plots of (a) log (1,2,7-TMN/1,3,7-TMN) vs. log (1,2,5-TMN/1,3,6-TMN), (b) log (1,2,5-TMN/1,3,6-TMN) vs. log (1-MP/9-MP), and (c) log (1,7-DMP/(1,3- + 3,9- + 2,0- + 3,10-DMP)) vs. log (Retene/9-MP) of the sediments from the Shizigou Formation in the Yiliping Depression, Qaidam Basin, China.

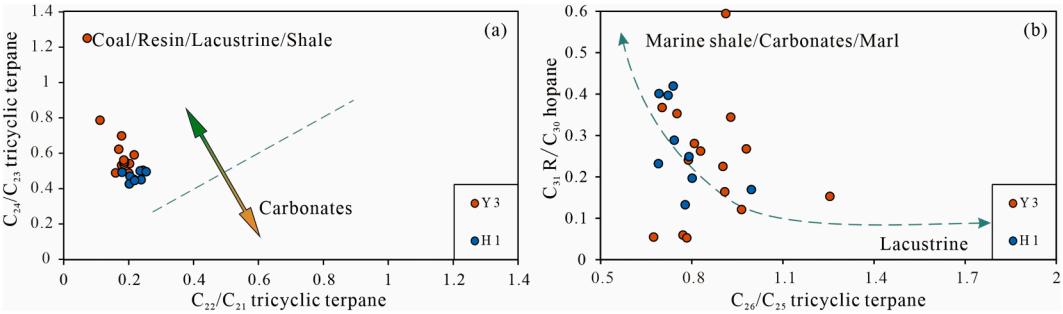

Fig. 10. Cross plots of (a) C_{22}/C_{21} vs. C_{24}/C_{23} tricyclic terpane and (b) C_{26}/C_{25} tricyclic terpane vs. $C_{31}R/C_{30}$ hopane of the sediments from the Shizigou Formation in the Yiliping Depression, Qaidam Basin, China (modified after Peters et al., 2005).

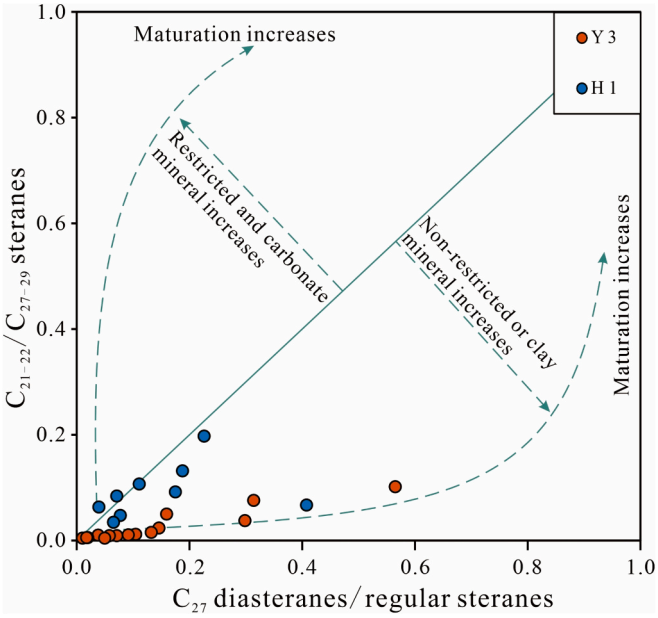

Fig. 11. Cross plot of C_{27} diasteranes/regular steranes vs. C_{21-22}/C_{27-29} steranes, showing the depositional setting for the sediments from the Shizigou Formation in the Yiliping Depression, Qaidam Basin, China.

oxygen-rich environments above from oxygen-depleted sediments below (Pawlowska et al., 2013; Blumenberg et al., 2015; Lee et al., 2019) and lead to localized reducing conditions in microenvironments beneath microbial mats (i.e., "mat-seal effect") (Pawlowska et al., 2013). Moreover, the interpretation of more reducing conditions is supported by the presence of halophilic bacteria which contribute to phytane in hypersaline environments (see 5.3.2) (Ten Haven et al., 1987; Qiao et al., 2021a). The farnesane (*i*-C_{15}) and aryl isoprenoids, serving as indicators of green sulfur bacteria (Summons and Powell, 1987), which are strictly anaerobic photosynthetic bacteria, show negligible concentrations illustrating the non-existence of reducing bottom water conditions. Additionally, oxic conditions are also supported by the relatively low $(S_1 + S_2)$/TOC ratios and S_2/S_3 ratios (Table 1) (Kumar et al., 2021).

In summary, the paleoredox conditions of the water column were oxic in most cases, but some samples with high TOC content from the Y 3 well were deposited under dyoxic conditions within the study area.

5.3.2. *Paleosalinity*

The increase in water salinity generally has an adverse impact on biodiversity, while simultaneously favoring the preservation of OM following deposition (Romero-Viana et al., 2012; Qiao et al., 2021a and b).

The analysis of the TOC/TS ratio (Fig. 13a) (Berner and Raiswell, 1984) reveals that the studied samples were predominantly deposited in saline to the hypersaline environments. It is observed that many late Neogene samples are positioned to the left of the TOC/TS = 0.5 line (Fig. 13a), while the majority of the Pleistocene samples are located to the right of the line (Fig. 9a in Qiao et al., 2021a), indicating that the paleosalinity during deposition of the late Neogene sediments was higher than during the Pleistocene in the lake. This finding is corroborated by biomarkers, which indicate a hypersaline environment characterized by high ratios of Gamm/C_{30} ($\alpha\beta + \beta\beta$) hopane (Fig. 13b; Table 3). Additionally, a high ETR is indicative of reducing situations and/or high salinity conditions in the water column, and an indicator of algal contribution to primary productivity (Hao et al., 2009; Hao et al., 2011; Volkman et al., 2015). For the studied sample, the high values of ETR are primarily attributed to the high salinity in the water column because of the dyoxic condition in the aquatic environment as mentioned above (Fig. 13b). The appearance of β-carotane has been widely recognized as a reliable marker for high salinity conditions (Peters et al., 2005; Liu et al., 2023b). However, the studied samples show a low abundance of β-carotane which might be due to the low maturity. In addition, C_{30} lanostane can be identified, which is inductive of high salinity conditions. Additionally, the high HD/D ratio further supports the inference of high salinity in the studied samples (Fan et al.,

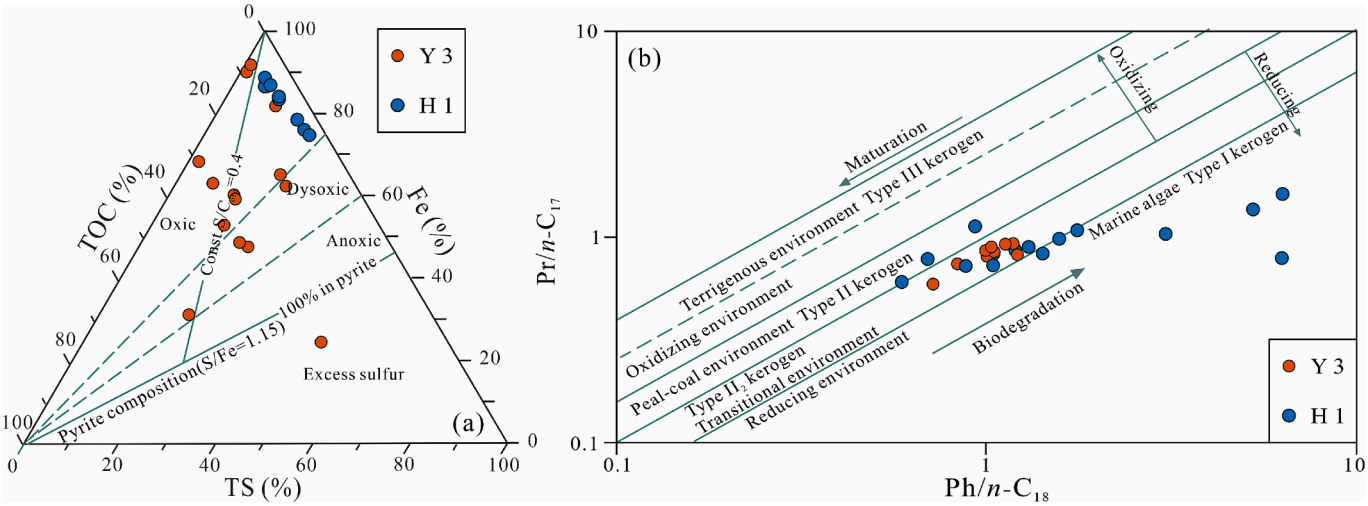

Fig. 12. (a) Ternary diagram of the relative concentration of TOC-TS-iron and (b) cross plot of pristane/*n*-C_{17} vs. phytane/*n*-C_{18} showing paleoredox conditions for the sediments from the Shizigou Formation in the Yiliping Depression, Qaidam Basin, China.

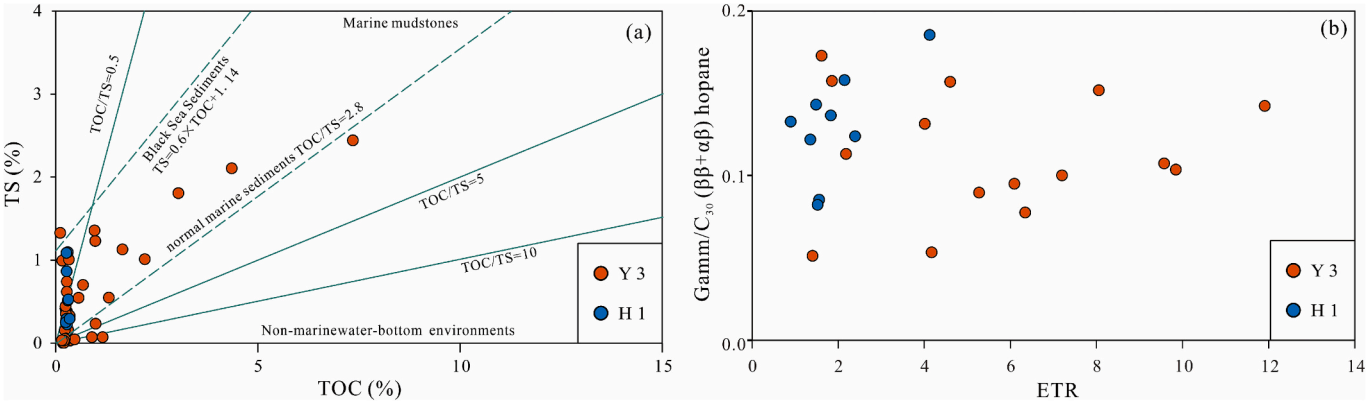

Fig. 13. Cross plots of (a) TS vs. TOC and (b) extended tricyclic terpane ratio vs. gammacerane/C_{30} αβ hopane indicating paleosalinity conditions for the sediments from the Shizigou Formation in the Yiliping Depression, Qaidam Basin, China.

1991; Al-Arouri et al., 1998). Furthermore, the MTTC ratio (α-MTTC/total-MTTCs) serves as a reliable indicator of paleosalinity (Schwark et al., 1998) with ratios of <0.5 and >0.5 indicating hypersaline and mesosaline environments, respectively (Schwark et al., 1998). In conjunction with the value of Pr/Ph, Fig. 14a indicates that the studied samples from the H 1 well were mainly deposited under a mesosaline environment, while the samples from the Y 3 well were primarily formed under conditions with salinity similar to that of a normal marine environment (Peters et al., 2005). The same results can be drawn from the relationship between DBT/PHE and Pr/Ph (Fig. 14b). The detectable hop-17 (21)-enes also indicate the prevalence of hypersaline conditions because they are minor to absent in sediments formed under normal salinity (Riboulleau et al., 2007).

The difference in paleosalinity between samples from the H 1 well and Y 3 well can be further supported by the molecular maturity-related parameters because paleosalinity conditions of water columns play a crucial role in influencing these parameters. It has been observed that immature extracts from hypersaline rocks exhibit a higher thermal maturity stage in the molecular maturity-related parameters of ββ/(ββ + αα) and ααα20S/(20S + 20R) steranes, as well as 22S/(22S + 22R) hopanes (Fig. 15a; Table 3) (Ten Haven et al., 1986; Rullkötter et al., 1994). The TAS cracking ratio (i.e., (C_{20} + C_{21})/(C_{20} + C_{21} + C_{26} + C_{27} + C_{28})) and C_{20}/(C_{20} + C_{28} (20R)) TAS ratio are commonly used as maturity indicators (Hegazi and El-Gayar, 2009; Thompson-Butler et al., 2019), indicating the immaturity for the most samples (Fig. 15b). However, as the aforementioned aliphatic hydrocarbon maturity-related parameters, the samples from hypersaline rocks show a higher thermal maturity stage (Fig. 15b). It should be noted that the difference in paleosalinity between samples from the H 1 well and Y 3 well is consistent with the lithologic composition of the samples, i.e., the samples from the H 1 well contain more carbonates (Figs. 10a and 11).

DBTs, DBFs, and Fs (Fig. 16) could be formed by reactions of biphenyl or methyl substituted biphenyls with surface active sulfur, oxygen, and methylene species on carbon surfaces (Asif et al., 2010). It is suggested that DBTs are abundant in source rocks deposited in saline water, compared to their oxygen-heterocyclic counterparts DBFs, which tend to prevail in freshwater (Pu et al., 1990; Fan et al., 1991). The brackish/hypersaline vs. lacustrine situation can be evaluated by the triangular diagram of Fl-DBF-DBT (Fig. 16). Considering the oxygen-rich depositional environment for the samples from the H 1 well, the triangular diagram indicates that the paleosalinity for the H 1 well was high. Due to the rise of the Qinghai-Tibetan Plateau, the Qaidam Basin experienced a prolonged period of drying and cooling during the Cenozoic era (Zhuang et al., 2011; Cai et al., 2012; Zhang et al., 2013), which facilitated the development of shallow-water evaporitic environments, where the OM was primarily composed of microbial and algal organisms (Warren, 1986; Goodarzi, 2020b). Moreover, the elevation of the East Qinghai-Tibetan Plateau has reached more than 4 km since the Neogene (Ding et al., 2022). A lake that can sustainably survive must receive additional water inflow, either due to rainfall, from rivers or

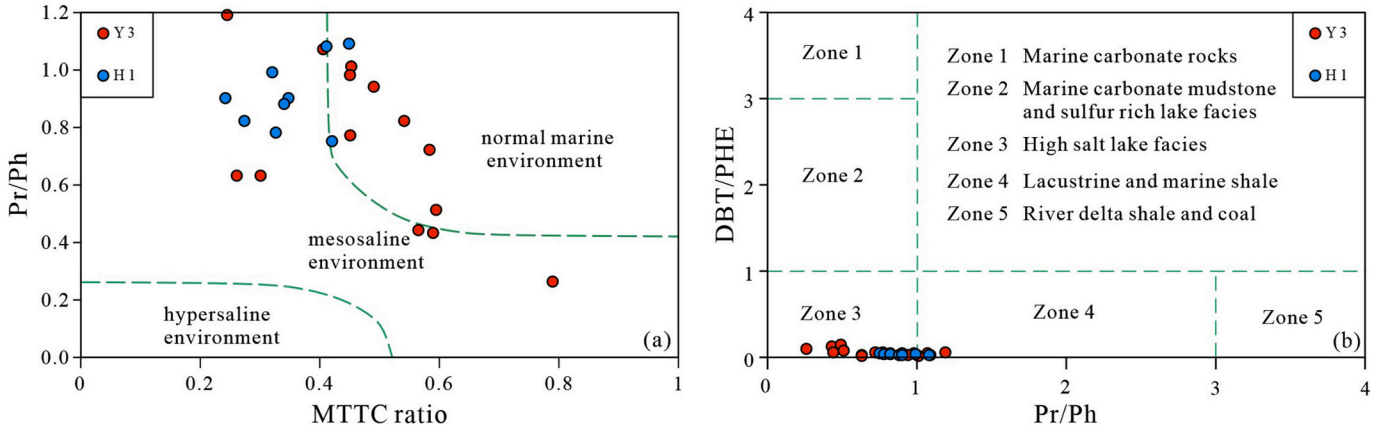

Fig. 14. Cross plots of (a) pristane/phytane vs. methyltrimethyltridecylchroman (MTTC) ratio and of (b) dibenzothiophene/phenanthrene ratio vs. pristane/phytane ratio, reflecting depositional environment of the sediments from the Shizigou Formation in the Yiliping Depression, Qaidam Basin, China.

glacial meltwater. These sources of freshwater can alter the lake's salinity, resulting in a situation where the marginal and shallower areas receive freshwater from rivers and meltwater, while the central and deeper sections are more saline and potentially stratified. In view of the altitude, it is unlikely that in the enhanced salinity is a result of marine transgression.

Generally speaking, the samples from the H 1 well (the central area) were deposited under higher paleosalinites (mesosaline) than the samples from the Y 3 well (the marginal area). However, even there salinities were significantly higher than in "normal" freshwater.

It should be emphasized that the Pleistocene samples show lower DBT concentrations compared to the late Neogene samples (Fig. 9a in Qiao et al., 2021a), indicating differences in paleosalinity between the late Neogene and the Pleistocene sediments mentioned above. The higher paleosalinity might be the reason for the lower degree of biodegradation in the OM (see section 5.4) (Grassia et al., 1996).

5.4. Evidence of biodegradation

The occurrence of biodegradation in OM within sediments is fundamental to assessing the potential for microbial gas generation. Although there is some indirect evidence that biodegradation has occurred, such as low HI and $CPI_{24–34}$ values, more direct evidence needs to be provided. On the one hand, there is a discrepancy between the strong input from algae and bacteria (based on biomarker data) and comparatively low HI values. While hydrogen-rich algae are supposed to be resistant to degradation (Derenne et al., 1990; Derenne et al., 1991), it is known that degradation can reduce HI values significantly

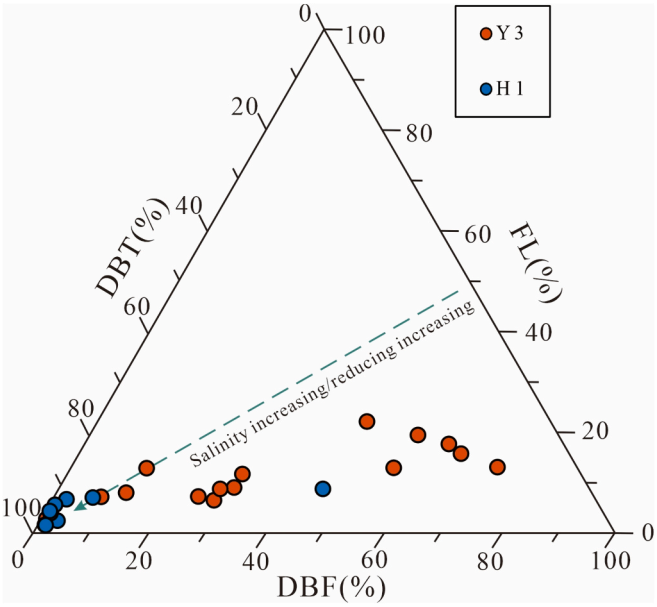

Fig. 16. Relative proportions of fluorene (FL), dibenzofuran (DBF), and dibenzothiophene (DBT) indicating paleosalinity conditions for the sediments from the Shizigou Formation in the Yiliping Depression, Qaidam Basin, China.

(Horsfield et al., 1994). Consequently, the algae in these samples might

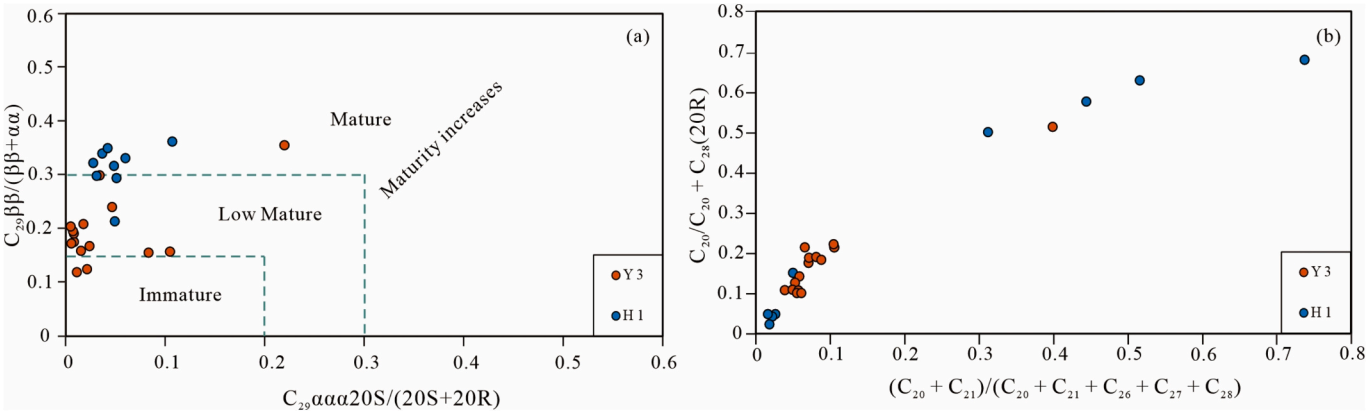

Fig. 15. Thermal maturity indicators of (a) C_{29} ααα 20S/(20S + 20R) vs. C_{29} ββ/(ββ + αα) steranes and (b) $(C_{20} + C_{21})/(C_{20} + C_{21} + C_{26} + C_{27} + C_{28})$ vs. $C_{20}/(C_{20} + C_{28}$ (20R)) triaromatic steroids.

be biodegraded. On the other hand, Fig. 3a and b shows a transition occurred from ulminite to bituminite (very dark huminite), which might indicate degraded humic matter in terrestrial environments (Kus et al., 2017).

The primary stages of biodegradation (rank 1–2) are characterized by the preferential removal of *n*-alkanes ranging between C_8 and C_{12} (Peters et al., 2005). The heavy degree (rank 3) of biodegradation of OM is characterized by the complete absence of *n*-alkanes $<C_{16}$ while the complete depletion of *n*-alkanes ranging from $<C_{15}$ to C_{35} is inductive of severe microbial degradation (rank >3) (Peters et al., 2005). The samples from the H 1 well show sparse concentrations of *n*-alkanes with a chain length of less than 16, while those from the Y 3 well show nonexistence of *n*-alkanes with a carbon number less than 15. These observations signify a moderate (rank 2) to heavy level of biodegradation for the studied samples. In addition, isoprenoids, such as norpristane, Pr and Ph, show high concentrations in the studied samples, which indicates that isoprenoids are not affected by biodegradation and the level of biodegradation is smaller than 5, as complete consumption of isoprenoids occurs at ranks >4. Furthermore, the presence of unresolved complex mixture (UCM) in the total ion chromatogram (TIC) (Fig. 4a and b) readily indicates the occurrence of biodegradation (Blumer et al., 1973; Peters et al., 2005).

Moreover, the C_{29} NH/C_{30} αβ hopane ratios exceeding 0.10 in 50% of the samples suggest heavy to severe biodegradation (4< rank <5) in these samples. In light of the aforementioned evidence, it can be inferred that the degradation of the OM is rated at a level of 3 to 4 in the study area. Additionally, alkylated PAH isomers show a varying susceptibility to biodegradation, which generally decreases with the increase in the number of alkyl substituents (Peters et al., 2005). The dimethylnaphthalene ratio, trimethylnaphthalene ratio, and tetramethylnaphthalene ratio support that the degradation levels are smaller than 4 in most cases (Table 4) (Peters et al., 2005). The degree of the OM degradation in the Pleistocene sediments was not assessed by Qiao et al. (2021a). However, based on the higher C_{29} NH/C_{30} αβ hopane ratios in the Pleistocene samples, it is assumed that the degree of the OM biodegradation in the late Neogene sediments is lower compared to that in the Pleistocene samples. In summary, considering the geologic conditions including low thermal maturity, origin of OM, and sedimentary environment, there is clear evidence of biodegradation in the late Neogene sediments similar to that in the Pleistocene Qigequan Formation, which is the most important target for microbial gas exploration and exploitation (check Qiao et al., 2021a and 2022 for detail). Probably, the late Neogene Shizigou Formation in the Yiliping Depression has also substantial potential for microbial generation.

6. Conclusions

The new elemental, organic geochemical and petrographic data gleaned from the late Neogene Shizigou Formation of the Qaidam Basin in China supply significant insights encompassing the depositional environment, biological sources, and the level of biodegradation of organic matter (OM). These findings contribute to the existing geological knowledge of the region and offer pertinent implications for the further exploration of microbial gas.

(1) During the late Neogene period, the Qaidam Basin witnessed the deposition of prospective microbial gas source rocks characterized by low-moderate total organic carbon (TOC) content. In the marginal area around the Y 3 well, a salinity similar to normal marine conditions developed, with the presence of dysoxic (the samples with high TOC content) to oxic bottom-water conditions. In contrast, in the area of the H 1 well a mesosaline environment prevailed characterized by the presence of oxic bottom-water conditions. Water stratification did not exist and thus no persistent anoxic bottom water layer developed. Generally, the salinity of the late Neogene lake was higher than that of the Pleistocene lake.

(2) At the margin of the depression around the Y 3 well both high TOC and low TOC samples occur. The former are primarily composed of a combination of huminite, semifusinite, fusinite, resinite, sporinite, lamalginite, and liptodetrinite. In contrast, the samples with low TOC content from both the Y 3 and H 1 wells have a simpler maceral composition consisting of huminite, lamalginite, and liptodetrinite. The petrographic data indicate predominance of higher plant material for the TOC-rich samples, and less higher plant contribution for the TOC-lean samples from both the Y 3 and H 1 wells. Most of the samples are thermally immature. The molecular data indicate that the biological sources of the OM in the central area of the depression (the H 1 well) were relatively uniform, i.e., mainly saltwater algae and bacteria, while the OM origin in the marginal area of the depression is more diverse, including algae, bacteria, and various aquatic higher plants (in the Y 3 well). Terrestrial higher plants, primarily angiosperms, contribute little to the OM in all samples based on biomarker data. The late Neogene Shizigou Formation exhibits a prominent occurrence of emergent macrophytes but a reduced abundance of lower aquatic organisms (algae) compared to the Pleistocene Qigequan Formation.

(3) While the Shizigou Formation possesses a lower potential for hydrocarbon generation and shows a lower degree of biodegradation in OM compared to the Pleistocene Qigequan Formation, there is nevertheless a significant potential for microbial gas generation due to the great thickness of the layer and the rapid deposition in the Yiliping Depression.

CRediT authorship contribution statement

Jinqi Qiao: Writing – review & editing, Writing – original draft, Project administration, Funding acquisition, Formal analysis, Data curation. **Qingyong Luo:** Writing – original draft, Supervision, Methodology, Conceptualization. **Shouxin Guo:** Visualization. **Xianglu Tang:** Resources, Investigation. **Ludmila Kopaevich:** Writing – original draft, Methodology. **Ralf Littke:** Writing – review & editing, Writing – original draft, Methodology, Conceptualization.

Declaration of competing interest

We hereby confirm that all authors agreed on submission of this manuscript, that this work has not been published or submitted elsewhere, and that there aren't any other conflicts of interest.

Data availability

Data will be made available on request.

Acknowledgement

This work was jointly financially supported by the National Natural Science Foundation of China (No. 42202154) and Science Foundation of China University of Petroleum, Beijing (No. ZX20220074). We thank two reviewers for their constructive comments which greatly helped to improve the manuscript.

Appendix A

Terpanes (*m/z* 191)		
Peak	Abbreviation	Biomarker
A	C_{19} Tri	C_{19} tricyclic terpane
B	C_{20} Tri	C_{20} tricyclic terpane
C	C_{21} Tri	C_{21} tricyclic terpane
D	C_{22} Tri	C_{22} tricyclic terpane
E	C_{23} Tri	C_{23} tricyclic terpane
F	C_{24} Tri	C_{24} tricyclic terpane
G	C_{25} Tri	C_{25} tricyclic terpane
H	C_{24} TeT	C_{24} tetracylic terpane
I	C_{26} Tri R	C_{26} R tricyclic terpane
	C_{26} Tri S	C_{26} S tricyclic terpane
J	C_{28} Tri R	C_{28} R tricyclic terpane
	C_{28} Tri S	C_{28} S tricyclic terpane
K	C_{29} Tri R	C_{29} R tricyclic terpane
	C_{29} Tri S	C_{29} S tricyclic terpane
1	Ts	C_{27} 18α (H) -22,29,30-trisnorneohopane
2	Tm	C_{27} 17α (H) -22,29,30-trisnorhopane
3	βTm	C_{27} 17β (H) -22,29,30-trisnorhopane
4	C_{29} NH	C_{29} 17α (H),21β (H)-25-norhopanes
5	C_{29} neoH	C_{29} neohop-13 (18)-ene
6	C_{29} αβ hopane	C_{29} 17α (H),21β (H)-30-norhopane
7	C_{29} Ts	C_{29} 18α (H) -30-norneohopane
8	C_{30} H 17 (21)	C_{30} hop-17 (21) -ene
9	C_{29} βα hopane	C_{29} 17β (H),21α (H) -norhopane
10	Ole	Oleanane
11	C_{30} αβ hopane	C_{30} 17α (H),21β (H) -hopane
12	C_{30} neo hopane	C_{30} neohop-13 (18) -enes
13	C_{29} ββ hopane	C_{29} 17β (H),21β (H) -norhopane
14	C_{31} αβ hopane S	C_{31}-17α (H),21β (H),22S-homohopane
	C_{31} αβ hopane R	C_{31}-17α (H),21β (H),22R-homohopane
15	Gamm	Gammacerane
16	C_{30} ββ hopane	C_{30} 17β (H),21β (H) -hopane
17	C_{32} αβ hopane S	C_{32} 17α (H),21β (H),22S-homohopane
	C_{32} αβ hopane R	C_{32} 17α (H),21β (H),22R-homohopane
18	C_{31} ββ hopane	C_{31} 17β (H),21β (H) -homohopane
19	C_{33} αβ hopane S	C_{33} 17α (H),21β (H),22S-homohopane
	C_{33} αβ hopane R	C_{33} 17α (H),21β (H),22R-homohopane
20	C_{32} ββ hopane	C_{32} 17β (H),21β (H) -homohopane
21	C_{34} αβ hopane S	C_{34} 17α (H),21β (H),22S-homohopane
	C_{34} αβ hopane R	C_{34} 17α (H),21β (H),22R-homohopane
22	C_{35} αβ hopane S	C_{35} 17α (H),21β (H),22S-homohopane
	C_{35} αβ hopane R	C_{35} 17α (H),21β (H),22R-homohopane

Steranes (*m/z* 217)		
Peak	Abbreviation	Biomarker
a	Pregnane	5α,14β,17β (H) -pregnane (diginane)
b	Homopregnane	5α,14β,17β (H) -homopregnane (20-methyldiginane)
c	C_{27} ααα20S	20S-5α (H), 14α (H), 17α (H) -cholestane
d	C_{27} αββ20R	20R-5α (H), 14β (H), 17β (H) -cholestane
e	C_{27} αββ20S	20S-5α (H), 14β (H), 17β (H) -cholestane
f	C_{27} ααα20R	20R-5α (H), 14α (H), 17α (H) -cholestane
g	C_{28} ααα20S	20S-24-Methyl-5α (H), 14α (H), 17α (H) -cholestane
h	C_{28} αββ20R	20R-24-Methyl-5α (H), 14β (H), 17β (H) -cholestane
i	C_{28} αββ20S	20S-24-Methyl-5α (H), 14β (H), 17β (H) -cholestane
j	C_{28} ααα20R	20R-24-Methyl-5a (H), 14a (H), 17a (H) -cholestane
k	C_{29} ααα20S	20S-24-Ethyl-5α (H), 14α (H), 17α (H) - cholestane
l[a]	C_{29} αββ20R	20R-24-Ethyl-5α (H), 14β (H), 17β (H) -cholestane
m	C_{29} αββ20S	20S-24-Ethyl-5α (H), 14β (H), 17β (H) - cholestane
n	C_{29} ααα20R	20R-24-Ethyl-5α (H), 14α (H), 17α (H) -cholestane

[a] 24-Ethyl-5β (H), 14β (H), 17β (H) -cholestane exists and co-elutes with peaks labeled by l.

References

Ahad, J.M., Ganeshram, R.S., Bryant, C.L., Cisneros-Dozal, L.M., Ascough, P.L., Fallick, A.E., Slater, G.F., 2011. Sources of n-alkanes in an urbanized estuary: Insights from molecular distributions and compound-specific stable and radiocarbon isotopes. Mar. Chem. 126 (1–4), 239–249.

Al-Arouri, K.R., Mckirdy, D.M., Boreham, C.J., 1998. Oil-source correlations as a tool in identifying the petroleum systems of the southern Taroom Trough, Australia. Org. Geochem. 29 (1–3), 713–734.

Alexander, R., Kagi, R.I., Woodhouse, G.W., Volkman, J.K., 1983. The geochemistry of some biodegraded Australian oils. Aust. Petrol. Explor. Assoc. J. 23, 53–63.

Alexander, R., Kagi, R.I., Noble, R., Volkman, J.K., 1984. Identification of some bicyclic alkanes in petroleum. Org. Geochem. 6, 63–72.

Amo, M., Suzuki, N., Shinoda, T., Ratnayake, N.P., Takahashi, K., 2007. Diagenesis and distribution of sterenes in late Miocene to Pliocene marine siliceous rocks from Horonobe (Hokkaido, Japan). Org. Geochem. 38 (7), 1132–1145.

Armstroff, A., Wilkes, H., Schwarzbauer, J., Littke, R., Horsfield, B., 2006. Aromatic hydrocarbon biomarkers in terrestrial organic matter of Devonian to Permian age. Palaeogeogr. Palaecolimatol. Palaeoecol. 240 (1–2), 253–274.

Asif, M., Alexander, R., Fazeelat, T., Grice, K., 2010. Sedimentary processes for the geosynthesis of heterocyclic aromatic hydrocarbons and fluorenes by surface reactions. Org. Geochem. 41 (5), 522–530.

Bauersachs, T., Kremer, B., Schouten, S., Sinninghe Damsté, J.S., 2009. A biomarker and δ15N study of thermally altered Silurian cyanobacterial mats. Org. Geochem. 40 (2), 149–157.
Bechtel, A., Gruber, W., Sachsenhofer, R.F., Gratzer, R., Püttmann, W., 2001. Organic geochemical and stable carbon isotopic investigation of coals formed in low-lying and raised mires within the Eastern Alps (Austria). Org. Geochem. 32 (11), 1289–1310.
Bechtel, A., Widera, M., Sachsenhofer, R.F., Gratzer, R., Lücke, A., Woszczyk, M., 2007. Biomarker and stable carbon isotope systematics of fossil wood from the second Lusatian lignite seam of the Lubstów deposit (Poland). Org. Geochem. 38 (11), 1850–1864.
Bechtel, A., Jia, J., Strobl, S.A., Sachsenhofer, R.F., Liu, Z., Gratzer, R., Püttmann, W., 2012. Palaeoenvironmental conditions during deposition of the Upper Cretaceous oil shale sequences in the Songliao Basin (NE China): Implications from geochemical analysis. Org. Geochem. 46, 76–95.
Bechtel, A., Movsumova, U., Strobl, S.A., Sachsenhofer, R.F., Soliman, A., Gratzer, R., Püttmann, W., 2013. Organofacies and paleoenvironment of the Oligocene Maikop series of Angeharan (eastern Azerbaijan). Org. Geochem. 56, 51–67.
Behar, F., Delhaye-Prat, V., Garel, S., 2021. Detrital input quantification in lacustrine petroleum systems: an example of the pre-salt source rocks from the lower Congo Basin (Congo). Depos. Rec. 7 (1), 147–171.
Berner, R.A., Raiswell, R., 1984. C/S method for distinguishing freshwater from marine sedimentary rocks. Geology 12 (6), 365–368.
Beti, D.R., Garel, S., Setoyama, E., Behar, F., Ring, T.A., Kanungo, S., 2021. A new resource assessment workflow to achieve gas risk and phase-specific source potential indices. Mar. Pet. Geol. 105136.
Bingham, E.M., McClymont, E.L., Väliranta, M., Mauquoy, D., Roberts, Z., Chambers, F. M., Pancost, R.D., Evershed, R.P., 2010. Conservative composition of n-alkane biomarkers in Sphagnum species: implications for palaeoclimate reconstruction in ombrotrophic peat bogs. Org. Geochem. 41 (2), 214–220.
Blumenberg, M., Thiel, V., Reitner, J., 2015. Organic matter preservation in the carbonate matrix of a recent microbial mat–is there a 'mat seal effect'? Org. Geochem. 87, 25–34.
Blumer, M., Ehrhardt, M., Jones, J.H., 1973. The environmental fate of stranded crude oil. Deep-Sea Res. 20, 239–259.
Bottari, F., Marsili, A., Morelli, I., Pacchiani, M., 1972. Aliphatic and triterpenoid hydrocarbons from ferns. Phytochemistry 11 (8), 2519–2523.
Bourbonniere, R.A., Meyers, P.A., 1996. Anthropogenic influences on hydrocarbon contents of sediments deposited in eastern Lake Ontario since 1800. Environ. Geol. 28, 22–28.
Bray, E.E., Evans, E.D., 1961. Distribution of n-paraffins as a clue to recognition of source beds. Geochim. Cosmochim. Acta 22, 2–15.
Budzinski, H., Garrigues, P.H., Connan, J., Devillers, J., Domine, D., Radke, M., Oudins, J.L., 1995. Alkylated phenanthrene distributions as maturity and origin indicators in crude oils and rock extracts. Geochim. Cosmochim. Acta 59, 2043–2056.
Cai, M., Fang, X., Wu, F., Miao, Y., Appel, E., 2012. Pliocene–Pleistocene stepwise drying of Central Asia: evidence from paleomagnetism and sporopollen record of the deep borehole SG-3 in the western Qaidam Basin, NE Tibetan Plateau. Global Planet. Change 94, 72–81.
Carroll, A.R., Wartes, M.A., 2003. Organic Carbon Burial by Large Permian Lakes, Northwest China. 370. Geological Society of America Special Paper, pp. 91–104.
Chaffee, A.L., Fookes, C.J.R., 1988. Polycyclic aromatic hydrocarbons in Australian coals—III, Structural elucidation by proton nuclear magnetic resonance spectroscopy. Org. Geochem. 12, 261–271.
Chaffee, A.L., Johns, R.B., 1983. Polycyclic aromatic hydrocarbons in Australian coals, I. Angularly fused pentacyclic tri-and tetraaromatic components of Victorian brown coal. Geochim. Cosmochim. Acta 47, 2141–2155.
Cichon-Pupienis, A., Littke, R., Lazauskienė, J., Baniasad, A., Pupienis, D., Radzevičius, S., Šiliauskas, L., 2021. Geochemical and sedimentary facies study–Implication for driving mechanisms of organic matter enrichment in the lower Silurian fine-grained mudstones in the Baltic Basin (W Lithuania). Int. J. Coal Geol. 244, 103815.
Clark, R.C., Blumer, M., 1967. Distribution of n-paraffins in marine organisms and sediment 1. Limnol. Oceanogr. 12 (1), 79–87.
Coetzee, J.A., 1967. Pollen analytical studies in East and Southern Africa. Palaeoecol. Afr. 3, 1–146.
Cranwell, P.A., 1977. Organic geochemistry of cam loch (Sutherland) sediments. Chem. Geol. 20, 205–221.
Demaison, G., Huizinga, B.J., 1991. Genetic classification of petroleum systems. AAPG Bull. 75, 1626–1643.
Derenne, S., Largeau, C., Casadevall, E., Sinninghe Damsté, J.S., Tegelaar, E.W., De, Leeuw J., W., 1990. Characterization of Estonian Kukersite by spectroscopy and pyrolysis: evidence for abundant alkyl phenolic moieties in an Ordovician, marine, type II/I kerogen. Org. Geochem. 16 (4–6), 873–888.
Derenne, S., Largeau, C., Casadevall, E., Berkaloff, C., Rousseau, B., 1991. Chemical evidence of kerogen formation in source rocks and oil shales via selective preservation of thin resistant outer walls of microalgae: origin of ultralaminae. Geochim. Cosmochim. Acta 55 (4), 1041–1050.
Didyk, B.M., Simoneit, B.R., Brassell, S.T., Eglinton, G., 1978. Organic geochemical indicators of palaeoenvironmental conditions of sedimentation. Nature 272 (5650), 216–222.
Ding, L., Kapp, P., Cai, F., Garzione, C.N., Xiong, Z., Wang, H., Wang, C., 2022. Timing and mechanisms of Tibetan Plateau uplift. Nat. Rev. Earth Environ. 3, 652–667.
dos Santos Neto, E.V., Hayes, J.M., Takaki, T., 1998. Isotopic biogeochemistry of the Neocomian lacustrine and Upper Aptian marine-evaporitic sediments of the Potiguar Basin, Northeastern Brazil. Org. Geochem. 28 (6), 361–381.
Ellis, L., Singh, R.K., Alexander, R., Kagi, R.I., 1996. Formation of isohexyl alkylaromatic hydrocarbons from aromatization-rearrangement of terpenoids in the sedimentary environment: a new class of biomarker. Geochim. Cosmochim. Acta 60 (23), 4747–4763.
Espitalié, J., Deroo, G., Marquis, F., 1985. La pyrolyse Rock-Eval et ses applications. Deuxième partie.Revue de l'Institut français du Pétrole. 40 (6), 755–784.
Fan, P., Philp, R.P., Li, Z., Yu, X., Ying, G., 1991. Biomarker distributions in crude oils and source rocks from different sedimentary environments. Chem. Geol. 93 (1–2), 61–78.
Farrimond, P., Talbot, H.M., Watson, D.F., Schulz, L.K., Wilhelms, A., 2004. Methylhopanoids: molecular indicators of ancient bacteria and a petroleum correlation tool. Geochim. Cosmochim. Acta 68 (19), 3873–3882.
Ficken, K.J., Li, B., Swain, D.L., Eglinton, G., 2000. An n-alkane proxy for the sedimentary input of submerged/floating freshwater aquatic macrophytes. Org. Geochem. 31 (7–8), 745–749.
Fu, J., Cunmin, P., Guoying, S., Dehan, L., Sizhong, C., 1993. A geochemical investigation of crude oils from eastern Pearl River mouth basin, South China Sea. L. SE. Asian Earth Sci. 8 (1–4), 469–486.
Gehrels, G., Kapp, P., DeCelles, P., Pullen, A., Blakey, R., Weislogel, A., Ding, L., Guynn, J., Martin, A., McQuarrie, N., Yin, A., 2011. Detrital zircon geochronology of pre-Tertiary strata in the Tibetan-Himalayan orogen. Tectonics 30 (5), TC5016.
Gonçalves, P.A., Kus, J., Hackley, P.C., Borrego, A.G., Hámor-Vidó, M., Kalkreuth, W., Mendonça Filho, J.G., Petersen, H.I., Pickel, W., Reinhardt, M.J., Suárez-Ruiz, I., ICCP, 2024. The petrology of dispersed organic matter in sedimentary rocks: Review and update. Int. J. Coal Geol. 104604.
Gong, L., Gao, X., Qu, F., Zhang, Y., Zhang, G., Zhu, J., 2023. Reservoir Quality and Controlling Mechanism of the Upper Paleogene Fine-Grained Sandstones in Lacustrine Basin in the Hinterlands of Northern Qaidam Basin, NW China. J. Earth Sci. 34 (3), 806–823.
Goodarzi, F., 2020a. Comparison of the geochemistry of lacustrine oil shales of Mississippian age from Nova Scotia and New Brunswick, Canada. Int. J. Coal Geol. 220, 103398.
Goodarzi, F., 2020b. A climate change event, detected in Viséan oil shales from Devon Island, Arctic Canada. Int. J. Coal Geol. 226, 103503.
Grassia, G.S., McLean, K.M., Glénat, P., Bauld, J., Sheehy, A.J., 1996. A systematic survey for thermophilic fermentative bacteria and archaea in high temperature petroleum reservoirs. FEMS Microbiol. Ecol. 21 (1), 47–58.
Grice, K., 2001. δ13C as an indicator of palaeoenvironments: a molecular approach. Stable Isotope Techniques in the Study of Biological Processes and Functioning of Ecosystems. 247–279.
Grice, K., Backhouse, J., Alexander, R., Marshall, N., Logan, G.A., 2005. Correlating terrestrial signatures from biomarker distributions, δ13C, and palynology in fluvio-deltaic deposits from NW Australia (Triassic–Jurassic). Org. Geochem. 36 (10), 1347–1358.
Grohmann, S., Romero-Sarmiento, M.F., Nader, F.H., Baudin, F., Littke, R., 2019. Geochemical and petrographic investigation of Triassic and late Miocene organic-rich intervals from onshore Cyprus, Eastern Mediterranean. Int. J. Coal Geol. 209, 94–116.
Haberer, R.M., Mangelsdorf, K., Wilkes, H., Horsfield, B., 2006. Occurrence and palaeoenvironmental significance of aromatic hydrocarbon biomarkers in Oligocene sediments from the Mallik 5L-38 Gas Hydrate Production Research well (Canada). Org. Geochem. 37 (5), 519–538.
Hao, F., Zhou, X., Zhu, Y., Yang, Y., 2009. Mechanisms for oil depletion and enrichment on the Shijiutuo uplift, Bohai Bay Basin, China. AAPG Bull. 93 (8), 1015–1037.
Hao, F., Zhou, X., Zhu, Y., Yang, Y., 2011. Lacustrine source rock deposition in response to co-evolution of environments and organisms controlled by tectonic subsidence and climate, Bohai Bay Basin, China. Org. Geochem. 42 (4), 323–339.
Harrison, T.M., Copeland, P., Kidd, W.S., Yin, A.N., 1992. Raising Tibet. Science 255 (5052), 1663–1670.
Hautevelle, Y., Michels, R., Malartre, F., Trouiller, A., 2006. Vascular plant biomarkers as proxies for palaeoflora and palaeoclimatic changes at the Dogger/Malm transition of the Paris Basin (France). Org. Geochem. 37 (5), 610–625.
He, D., Ladd, S.N., Saunders, C.J., Mead, R.N., Jaffé, R., 2020. Distribution of n-alkanes and their δ2H and δ13C values in typical plants along a terrestrial-coastal-oceanic gradient. Geochim. Cosmochim. Acta 281, 31–52.
Heermance, R.V., Pullen, A., Kapp, P., Garzione, C.N., Bogue, S., Ding, L., Song, P., 2013. Climatic and tectonic controls on sedimentation and erosion during the Pliocene–Quaternary in the Qaidam Basin (China). AAPG Bull. 125 (5–6), 833–856.
Hegazi, A.H., El-Gayar, M.S., 2009. Geochemical characterization of a biodegraded crude oil, Assran field, Central Gulf of Suez. J. Petrol. Geol. 32 (4), 343–355.
Holba, A.G., Ellis, L., Dzou, I.L., Hallam, A., Masterson, W.D., Francu, J., Fincannon, A.L., 2001. Extended tricyclic terpanes as age discriminators between Triassic, Early Jurassic, and Middle-Late Jurassic oils. In: (abs.) 20th International Meeting on Organic Geochemistry, Nancy-France, vol. 1, p. 464.
Horsfield, B., Curry, D.J., Bohacs, K., Littke, R., Rullkötter, J., Schenk, H.J., Radke, M., Schaefer, R.G., Carroll, A.R., Isaksen, G., Witte, E.G., 1994. Organic geochemistry of freshwater and alkaline lacustrine sediments in the Green River Formation of the Washakie Basin, Wyoming, USA. Org. Geochem. 22 (3–5), 415–440.
Huang, W.Y., Meinschein, W.G., 1979. Sterols as ecological indicators. Geochim. Cosmochim. Acta 43 (5), 739–745.
Huang, G., Pan, J., Xia, F., Yan, J., Zhang, C., Wu, D., Liu, Y., 2022. Provenance of uranium mineralization of the Yuqia area, Northwest China: Constraints from detrital zircon U-Pb geochronology and Hf isotopes. J. Earth Sci. 33 (6), 1549–1570.

Huang, H., Zhang, S., Su, J., 2015. Pyrolytically derived polycyclic aromatic hydrocarbons in marine oils from the Tarim Basin, NW China. Energ. Fuel. 29, 5578–5586.
Hughes, W.B., 1984. Use of thiophenic organic Sulphur compounds in characterizing of oils derived from carbonate versus siliciclastic sources. In: Palacas, G. (Ed.), Petroleum Geochemistry and Source Rock Potential of Carbonate Rocks, AAPG Studies in Geology, vol. 18, pp. 181–196.
ICCP, 1998. The new vitrinite classification (ICCP System 1994). Fuel 77, 349–358.
ICCP, 2001. The new inertinite classification (ICCP System 1994). Fuel 80, 459–471.
ISO 7404-2, 2009. Methods for the Petrographic Analysis of Coals - Part 2: Methods of Preparing Coal Samples. International Organization for Standardization, Geneva, Switzerland.
ISO 7404-3, 2009. Methods for the Petrographic Analysis of Coals - Part 3: Method of Determining Maceral Group Composition. International Organization for Standardization, Geneva, Switzerland.
ISO 7404–5, 2009. Methods for the Petrographic Analysis of Coal—Part 5: Methods of Determining Microscopically the Reflectance of Vitrinite. International Organization for Standardization, Geneva, Switzerland, 14 pp.
Jian, X., Guan, P., Zhang, W., Feng, F., 2013. Geochemistry of Mesozoic and Cenozoic sediments in the northern Qaidam basin, northeastern Tibetan Plateau: implications for provenance and weathering. Chem. Geol. 360, 74–88.
Jiang, C., Alexander, R., Kagi, R.I., Murray, A.P., 1998. Polycyclic aromatic hydrocarbons in ancient sediments and their relationships to palaeoclimate. Org. Geochem. 29 (5–7), 1721–1735.
Katz, B.J., 2011. Microbial processes and natural gas accumulations. Open Geol. J. 5, 75–83.
Kenig, F., 2000. C16–C29 homologous series of monomethylalkanes in the pyrolysis products of Holocene microbial mat. Org. Geochem. 31 (2–3), 237–241.
Killops, S.D., Abbott, G.D., 2022. On the origin of 3-methyl steroids and diasteranes. Chem. Geol. 607, 121014.
Kumar, D., Ghosh, S., Tiwari, B., Varma, A.K., Mathews, R.P., Chetia, R., 2021. Palaeocene-Eocene organic sedimentary archives of Bikaner-Nagaur Basin, Rajasthan, India: an integrated revelation from biogeochemical and elemental proxies. Int. J. Coal Geol. 247, 103848.
Kus, J., Araujo, C.V., Borrego, A.G., Flores, D., Hackley, P.C., Hámor-Vidó, M., Kalaitzidis, S., Kommeren, C.J., Kwiecińska, B., Mastalerz, M., Mendonça Filho, J.G., Menezes, T.R., Misz-Kennan, M., Nowak, G.J., Petersen, H.I., Rallakis, D., Suárez-Ruiz, I., Sýkorová, I., Životić, D., 2017. Identification of alginite and bituminite in rocks other than coal. 2006, 2009, and 2011 round robin exercises of the ICCP Identification of Dispersed Organic Matter Working Group. Int. J. Coal Geol. 178, 26–38.
Lee, C., Love, G.D., Jahnke, L.L., Kubo, M.D., Des Marais, D.J., 2019. Early diagenetic sequestration of microbial mat lipid biomarkers through covalent binding into insoluble macromolecular organic matter (IMOM) as revealed by sequential chemolysis and catalytic hydropyrolysis. Org. Geochem. 132, 11–22.
Littke, R., Klussmann, U., Krooss, B., Leythaeuser, D., 1991. Quantification of loss of calcite, pyrite, and organic matter due to weathering of Toarcian black shales and effects on kerogen and bitumen characteristics. Geochim. Cosmochim. Acta 55 (11), 3369–3378.
Liu, C., Jiang, Z., Li, J., Xie, Z., Jiang, G., Wang, J., 2011. Research on biogenetic gas reservoir formation of Shizigou FN on Pliocene in Yiliping of the Caidam Basin. Nature. Gas Ind 21 (6), 14–16 (In Chinese with English abstract).
Liu, S., Jiang, L., Liu, B., Zhao, C., Tang, S., Tan, F., 2023a. Investigation of organic matter sources and depositional environment changes for terrestrial shale succession from the yuka depression: implications from organic geochemistry and petrological analyses. J. Earth Sci. 34 (5), 1577–1595.
Liu, C., Chen, S., Zhao, J., Su, Z., Rong, H., 2022. Geochemical characteristics and origin of crude oil and natural gas in the Southern Slope Zone, Kuqa Foreland Basin, NW China. J. Earth Sci. 33 (3), 820–830.
Liu, S., Gao, G., Gang, W., Wang, B., Wang, M., Wang, C., 2023b. Comparison of formation conditions of source rocks of fengcheng and lucaogou formations in the junggar basin, nw china: implications for organic matter enrichment and hydrocarbon potential. J. Earth Sci. 34 (4), 1026–1040.
Lu, H., Sun, Y., 2003. Molecular and stable carbon isotopic composition of monomethylalkanes from one oil sand sample: source implications. Org. Geochem. 34 (6), 745–754.
Luo, Q., Gong, L., Qu, Y., Zhang, K., Zhang, G., Wang, S., 2018. The tight oil potential of the Lucaogou Formation from the southern Junggar Basin. China. Fuel. 234, 858–871.
Mackenzie, A.S., Patience, R.L., Maxwell, J.R., Vandenbroucke, M., Durand, B., 1980. Molecular parameters of maturation in the Toarcian shales, Paris Basin, France—I. Changes in the configurations of acyclic isoprenoid alkanes, steranes and triterpanes. Geochim. Cosmochim. Acta 44 (11), 1709–1721.
Mead, R., Xu, Y., Chong, J., Jaffé, R., 2005. Sediment and soil organic matter source assessment as revealed by the molecular distribution and carbon isotopic composition of n-alkanes. Org. Geochem. 36 (3), 363–370.
Meyers, P.A., Ishiwatari, R., 1995. Organic matter accumulation records in lake sediments. In: Physics and Chemistry of Lakes. Springer Berlin Heidelberg, Berlin, Heidelberg, pp. 279–328.
Moldowan, J.M., Sundararaman, P., Schoell, M., 1986. Sensitivity of biomarker properties to depositional environment and/or source input in the lower Toarcian of SW-Germany. Org. Geochem. 10 (4–6), 915–926.
Moldowan, J.M., Dahl, J., Huizinga, B.J., Fago, F.J., Hickey, L.J., Peakman, T.M., Taylor, D.W., 1994. The molecular fossil record of oleanane and its relation to angiosperms. Science 265 (5173), 768–771.
Nzoussi-Mbassani, P., Copard, Y., Disnar, J.R., 2005. Vitrinite recycling: diagnostic criteria and reflectance changes during weathering and reburial. Int. J. Coal Geol. 61 (3–4), 223–239.
Otto, A., Wilde, V., 2001. Sesqui-, di-, and triterpenoids as chemosystematic markers in extant conifers—a review. Bot. Rev. 67, 141–238.
Pang, X., Zhao, W., Su, A., Zhang, S., Li, M., Dang, Y., Xu, F., Zhou, R., Zhang, D., Xu, Z., Guan, Z., 2005. Geochemistry and origin of the giant Quaternary shallow gas accumulations in the eastern Qaidam Basin, NW China. Org. Geochem. 36 (12), 1636–1649.
Pawlowska, M.M., Butterfield, N.J., Brocks, J.J., 2013. Lipid taphonomy in the Proterozoic and the effect of microbial mats on biomarker preservation. Geology 41 (2), 103–106.
Pearson, A., Eglinton, T.I., 2000. The origin of n-alkanes in Santa Monica Basin surface sediment: a model based on compound-specific Δ14C and δ13C data. Org. Geochem. 31 (11), 1103–1116.
Pepper, A.S., Corvi, P.J., 1995. Simple kinetic models of petroleum formation. Part I: oil and gas generation from kerogen. Mar. Pet. Geol. 12 (3), 291–319.
Peters, K.E., Walters, C.C., Moldowan, J.M., 2005. The Biomarker Guide: Volume II Biomarkers and Isotopes in Petroleum Exploration and Earth History. Cambridge University Press, United Kingdom.
Philp, R.T., Gilbert, T.D., 1986. Biomarker distributions in Australian oils predominantly derived from terrigenous source material. Org. Geochem. 10 (1–3), 73–84.
Pickel, W., Kus, J., Flores, D., Kalaitzidis, S., Christanis, K., Cardott, B.J., Misz-Kennan, M., Rodrigues, S., Hentschel, A., Hamor-Vido, M., Crosdale, P.I., 2017. Classification of liptinite–ICCP System 1994. Int. J. Coal Geol. 169, 40–61.
Pu, F., Philip, R.P., Zhenxi, L., Guangguo, Y., 1990. Geochemical characteristics of aromatic hydrocarbons of crude oils and source rocks from different sedimentary environments. Org. Geochem. 16 (1–3), 427–435.
Qiao, J., Grohmann, S., Baniasad, A., Zhang, C., Jiang, Z., Littke, R., 2021a. High microbial gas potential of Pleistocene lacustrine deposits in the central Qaidam Basin, China: an organic geochemical and petrographic assessment. Int. J. Coal Geol. 245, 103818.
Qiao, J., Baniasad, A., Zieger, L., Zhang, C., Luo, Q., Littke, R., 2021b. Paleo-depositional environment, origin and characteristics of organic matter of the Triassic Chang 7 Member of the Yanchang Formation throughout the mid-western part of the Ordos Basin, China. Int. J. Coal Geol. 237, 103636.
Qiao, J., Littke, R., Grohmann, S., Zhang, C., Jiang, Z., Strauss, H., Zieger, L., 2022. Climatic and environmental conditions during the Pleistocene in the Central Qaidam Basin, NE Tibetan Plateau: evidence from GDGTs, stable isotopes and major and trace elements of the Qigequan Formation. Int. J. Coal Geol. 254, 103958.
Qiao, J., Luo, Q., Zhang, K., Zhang, G., Duan, J., Wang, D., Yu, H., Wang, S., Qu, Y., Kopaevich, L., 2023. Geochemistry and organic petrography of the Middle Permian Lucaogou alkaline lacustrine oil shale in the southern Junggar Basin, China: Implications for formation conditions and organic matter accumulation. Int. J. Coal Geol. 268, 104198.
Qiu, N., Kang, Y., Jin, Z., 2003. Temperature and pressure field in the Tertiary succession of the western Qaidam basin, Northeast Qinghai-Tibet Plateau, China. Mar. Pet. Geol. 20 (5), 493–507.
Radke, M., Vriend, S.P., Ramanampisoa, L.R., 2000. Alkyldibenzofurans in terrestrial rocks: influence of organic facies and maturation. Geochim. Cosmochim. Acta 64 (2), 275–286.
Riboulleau, A., Schnyder, J., Riquier, L., Lefebvre, V., Baudin, F., Deconinck, J.F., 2007. Environmental change during the Early Cretaceous in the Purbeck-type Durlston Bay section (Dorset, Southern England): a biomarker approach. Org. Geochem. 38 (11), 1804–1823.
Rice, D.D., Claypool, G.E., 1981. Generation, accumulation, and resource potential of biogenic gas. AAPG Bull. 65 (1), 5–25.
Rippen, D., Littke, R., Bruns, B., Mahlstedt, N., 2013. Organic geochemistry and petrography of Lower Cretaceous Wealden black shales of the Lower Saxony Basin: the transition from lacustrine oil shales to gas shales. Org. Geochem. 63, 18–36.
Romero-Sarmiento, M.F., Riboulleau, A., Vecoli, M., Versteegh, G., Laggoun-Défarge, F., 2011. Aliphatic and aromatic biomarkers from carboniferous coal deposits at Dunbar (east lothian, Scotland): palaeobotanical and palaeoenvironmental significance. Palaeogeogr. Palaeoclimatol. Palaeoecol. 309 (3), 309–326.
Romero-Viana, L., Kienel, U., Sachse, D., 2012. Lipid biomarker signatures in a hypersaline lake on Isabel Island (Eastern Pacific) as a proxy for past rainfall anomaly (1942–2006 AD). Palaeogeogr. Palaecolimatol. Palaeoecol. 350, 49–61.
Royden, L.H., Burchfiel, B.C., van der Hilst, R.D., 2008. The geological evolution of the Tibetan Plateau. Science 321 (5892), 1054–1058.
Rullkötter, J., Peakman, T.M., Ten Haven, H.L., 1994. Early diagenesis of terrigenous triterpenoids and its implications for petroleum geochemistry. Org. Geochem. 21 (3–4), 215–233.
Samad, S.K., Mishra, D.K., Mathews, R.P., Ghosh, S., Mendhe, V.A., Varma, A.K., 2020. Geochemical attributes for source rock and palaeoclimatic reconstruction of the Auranga Basin, India. J. Petrol. Sci. Eng. 185, 106665.
Schoell, M., 1980. The hydrogen and carbon isotopic composition of methane from natural gases of various origins. Geochim. Cosmochim. Acta 44 (5), 649–661.
Schwark, L., Vliex, M., Schaeffer, P., 1998. Geochemical characterization of Malm Zeta laminated carbonates from the Franconian Alb, SW-Germany (II). Org. Geochem. 29 (8), 1921–1952.
Scott, J.J., Buatois, L.A., Mangano, M.G., 2012. Lacustrine environments. In: Knaust, D., Bromley, R.G. (Eds.), Trace Fossils as Indicators of Sedimentary Environments. Developments in Sedimentology, vol. 64. Elsevier, Amsterdam, pp. 379–417.
Shiea, J., Brassell, S.C., Ward, D.M., 1990. Mid-chain branched mono-and dimethyl alkanes in hot spring cyanobacterial mats: a direct biogenic source for branched alkanes in ancient sediments? Org. Geochem. 15 (3), 223–231.

Simoneit, B.R., Grimalt, J.O., Wang, T.G., Cox, R.E., Hatcher, P.G., Nissenbaum, A., 1986. Cyclic terpenoids of contemporary resinous plant detritus and of fossil woods, ambers and coals. Org. Geochem. 10 (4–6), 877–889.
Sinninghe Damsté, J.S., Kenig, F., Koopmans, M.P., Köster, J., Schouten, S., Hayes, J.M., De Leeuw, J.W., 1995. Evidence for gammacerane as an indicator of water column stratification. Geochim. Cosmochim. Acta 59 (9), 1895–1900.
Sinninghe Damsté, J.S., Schouten, S., Volkman, J.K., 2014. C27–C30 neohop-13 (18) -enes and their saturated and aromatic derivatives in sediments: Indicators for diagenesis and water column stratification. Geochim. Cosmochim. Acta 133, 402–421.
Song, S., Huang, L., Zhang, Q., Li, X., Liu, C., 2022. New insights for origin of fine-grained sediments from the early neogene Qaidam Basin: Wind and fluvial–lacustrine source-to-sink processes. Mar. Pet. Geol. 145, 105853.
Strachan, M.G., Alexander, R., Kagi, R.I., 1988. Trimethylnaphthalenes in crude oils and sediments: effects of source and maturity. Geochim. Cosmochim. Acta 52 (5), 1255–1264.
Summons, R.E., Powell, T.G., 1987. Identification of aryl isoprenoids in source rocks and crude oils: biological markers for the green sulphur bacteria. Geochim. Cosmochim. Acta 51 (3), 557–566.
Sýkorová, I., Pickel, W., Christanis, K., Wolf, M., Taylor, G.H., Flores, D., 2005. Classification of huminite—ICCP System 1994. Int. J. Coal Geol. 62 (1–2), 85–106.
Synnott, D.P., Sanei, H., Dewing, K., Ardakani, O.H., Pedersen, P.K., 2017. Insight into visible light spectrum changes with increasing reflectance in bituminite and inertinite macerals. Fuel 197, 201–208.
Synnott, D.P., Schwark, L., Dewing, K., Percy, E.L., Pedersen, P.K., 2021. The diagenetic continuum of hopanoid hydrocarbon transformation from early diagenesis into the oil window. Geochim. Cosmochim. Acta 308, 136–156.
Synnott, D.P., Schwark, L., Dewing, K., Percy, E.L., Pedersen, P.K., 2023. The diagenetic continuum of steroid hydrocarbon transformation from early diagenesis into the oil window. Geochim. Cosmochim. Acta 342, 137–155.
Tapponnier, P., Zhiqin, X., Roger, F., Meyer, B., Arnaud, N., Wittlinger, G., Yang, J., 2001. Oblique stepwise rise and growth of the Tibet Plateau. Science 294 (5547), 1671–1677.
Ten Haven, H.L., De Leeuw, J.W., Peakman, T.M., Maxwell, J.R., 1986. Anomalies in steroid and hopanoid maturity indices. Geochim. Cosmochim. Acta 50 (5), 853–855.
Ten Haven, H.L., De Leeuw, J.W., Rullkötter, J., Sinninghe Damsté, J.S., 1987. Restricted utility of the pristane/phytane ratio as a palaeoenvironmental indicator. Nature 330 (6149), 641–643.
Thompson-Butler, William, Peters, K.E., Magoon, L.B., Scheirer, A.H., Moldowan, J.M., Blanco, V.O., Blanco, Vladimir Orlando, Gonzalez, R.E., Graham, S.A., Zumberge, J. E., Wavrek, D.A., et al., 2019. Identification of genetically distinct petroleum tribes in the Middle Magdalena Valley, Colombia. AAPG Bull. 103 (12), 3003–3034.
Tu, T.T., Derenne, S., Largeau, C., Mariotti, A., Bocherens, H., 2003. Comparison of leaf lipids from a fossil ginkgoalean plant and its extant counterpart at two degradation stages: diagenetic and chemotaxonomic implications. Rev. Palaeobot. Palyno. 124 (1–2), 63–78.
van Aarssen, B., Alexander, R., Kagi, R., 1996. The origin of Barrow Sub-basin crude oils: a geochemical correlation using land-plant biomarkers. The APPEA Journal 36, 465–476.
van Aarssen, B., Alexander, R., Kagi, R.I., 2000. Higher plant biomarkers reflect palaeovegetation changes during Jurassic times. Geochim. Cosmochim. Acta 64 (8), 1417–1424.
Volk, H., George, S.C., Middleton, H., Schofield, S., 2005. Geochemical comparison of fluid inclusion and present-day oil accumulations in the Papuan Foreland–evidence for previously unrecognised petroleum source rocks. Org. Geochem. 36 (1), 29–51.
Volkman, J., 2003. Sterols in microorganisms. Appl. Microbiol. Biotechnol. 60 (5), 495–506.
Volkman, J.K., Zhang, Z., Xie, X., Qin, J., Borjigin, T., 2015. Biomarker evidence for Botryococcus and a methane cycle in the Eocene Huadian oil shale, NE China. Org. Geochem. 78, 121–134.
Wakeham, S.G., 1990. Algal and bacterial hydrocarbons in particulate matter and interfacial sediment of the Cariaco Trench. Geochim. Cosmochim. Acta 54 (5), 1325–1336.
Warren, J.K., 1986. Shallow-water evaporitic environments and their source rock potential. J. Sediment. Petrol. 56, 442–454.
Wen, Z., Ruiyong, W., Radke, M., Qingyu, W., Guoying, S., Zhili, L., 2000. Retene in pyrolysates of algal and bacterial organic matter. Org. Geochem. 31 (7–8), 757–762.
Wu, Z., Grohmann, S., Littke, R., Guo, T., He, S., Baniasad, A., 2022. Organic petrologic and geochemical characterization of petroleum source rocks in the Middle Jurassic Dameigou Formation, Qaidam Basin, northwestern China: Insights into paleo-depositional environment and organic matter accumulation. Int. J. Coal Geol. 259, 104038.
Wu, Z., Littke, R., Baniasad, A., Yang, Z., Tang, Z., Grohmann, S., 2023. Geochemistry and petrology of petroleum source rocks in the Upper cretaceous Qingshankou Formation, Songliao Basin, NE China. Int. J. Coal Geol. 270, 104222.
Xiao, F., Yang, J.G., Li, S.C., Yao, Y.L., Huang, Y.M., Gao, X.Y., 2024. Enrichment and movability of lacustrine tight shale oil for the first member of the Upper cretaceous Qingshankou Formation in the Sanzhao Sag, Songliao Basin, NE China: Insights from saturated hydrocarbon molecules. Fuel 368, 131615.
Zhang, Z.G., Han, W.X., Fang, X.M., Song, C.H., Li, X.Y., 2013. Late Miocene–Pleistocene aridification of Asian inland revealed by geochemical records of lacustrine-fan delta sediments from the western Tarim Basin, NW China. Palaeogeogr. Palaeoclimatol. Palaeoecol. 377 (2), 52–61.
Zheng, T., Zieger, L., Baniasad, A., Grohmann, S., Hu, T., Littke, R., 2022. The Shahejie Formation in the Dongpu Depression, Bohai Bay Basin, China: Geochemical investigation of the origin, deposition and preservation of organic matter in a saline lacustrine environment during the Middle Eocene. Int. J. Coal Geol. 253, 103967.
Zhou, J., Xu, F., Wang, T., Cao, A., Yin, C., 2006. Cenozoic deformation history of the Qaidam Basin, NW China: Results from cross-section restoration and implications for Qinghai–Tibet Plateau tectonics. Earth Planet. Sci. Lett. 243 (1–2), 195–210.
Zhuang, G.S., Hourigan, J.K., Koch, P.L., Ritts, B.D., Kent-Corson, M.L., 2011. Isotopic constraints on intensified aridity in Central Asia around 12Ma. Earth Planet. Sci. Lett. 312 (1–2), 152–163.